Achieving μeV Tunneling Resolution in an In-Operando Scanning Tunneling Microscopy, Atomic Force Microscopy, and Magnetotransport System for Quantum Materials Research

Johannes Schwenk[1,2*], Sungmin Kim[1,2*], Julian Berwanger[3*], Fereshte Ghahari[1,2], Daniel Walkup[1,2], Marlou R. Slot[1,4], Son T. Le[1,5], William G. Cullen[1], Steven R. Blankenship[1], Sasa Vranjkovic[6], Hans J. Hug[6], Young Kuk[7], Franz J. Giessibl[3], and Joseph A. Stroscio[1†]

[1]Physical Measurement Laboratory, National Institute of Standards and Technology, Gaithersburg, MD 20899, USA
[2]Institute for Research in Electronics and Applied Physics, University of Maryland, College Park, MD 20742, USA
[3]Institute of Experimental and Applied Physics, University of Regensburg, 93053 Regensburg, Germany
[4]Department of Physics, Georgetown University, Washington, DC 20007, USA
[5]Theiss Research, La Jolla, CA 92037, USA
[6]Institute of Physics, University of Basel, Klingelbergstrasse 82, CH-4056 Basel, Switzerland
[7]Department of Physics and Astronomy, Seoul National University, Seoul 08826, Korea

Abstract: Research in new quantum materials requires multi-mode measurements spanning length scales, correlations of atomic-scale variables with macroscopic function, and spectroscopic energy resolution obtainable only at millikelvin temperatures, typically in a dilution refrigerator. In this article, we describe a multi-mode instrument achieving μeV tunneling resolution with *in-operando* measurement capabilities of scanning tunneling microscopy (STM), atomic force microscopy (AFM), and magnetotransport inside a dilution refrigerator operating at 10 mK. We describe the system in detail including a new scanning probe microscope module design, sample and tip transport systems, along with wiring, radio-frequency (RF) filtering, and electronics. Extensive benchmarking measurements were performed using superconductor-insulator-superconductor (SIS) tunnel junctions, with Josephson tunneling as a

[*] These authors contributed equally to this work.
[†] Corresponding author: joseph.stroscio@nist.gov

noise metering detector. After extensive testing and optimization, we have achieved less than 8 μeV instrument resolving capability for tunneling spectroscopy, which is 5-10 times better than previous instrument reports and comparable to the quantum and thermal limits set by the operating temperature at 10 mK.

I. Introduction

In today's frontier research, ultra-low temperature cryogenic instrumentation stands as a leading enabler of science as shown in fields ranging from quantum computing and information science [1,2], emergent quantum phases in materials research [3], to scanning probe microscopy (SPM) of future electronic materials [4]. STM was introduced in 1981 by Binnig and Rohrer [5,6] and is a variant of SPM that utilizes a tunneling sensor as compared to a force sensor in AFM [5]. A steady increase in sophistication in SPM instruments has occurred over the roughly four decades since the introduction of the technique, with a resurgence of instrumentation development into ultra-low temperature environments beginning in the early 2000s and increasing steadily since then [6–20]. Although SPM instruments have been developed that operate at temperatures down to ≈10 mK, none of them have achieved a tunneling energy resolution equivalent to their operating temperature. More typically, instruments show a noise-induced operating resolution equivalent to (150-200) mK [10,12,17,20,21], even though the instrument is operating at temperatures of almost ten times lower, although some progress has been made recently demonstrating tunneling resolutions below 100 mK [13,19]. In contrast, magnetotransport instruments deliver measurements with resolutions close to their base temperatures of (10-20) mK [22]. This discrepancy between SPM and magnetotransport instruments stems in part from the lack of electrical low-noise familiarity in the SPM community, which has progressed steadily in electrical transport measurements with demanding applications such as in quantum computation [23]. Other differences between the instruments include amplifier needs and electrical configurations. For example, in tunneling, a transimpedance amplifier operating at high gain is required, whereas electrical transport measurements typically rely on voltage amplifiers, which are commercially available for cryogenic environments.

In comparison with tunneling microscopes, the integration of force microscopy with dilution refrigerators has been even less common, although a number of instruments have been developed [7,24–27]. Combining AFM with STM opens up new capabilities in studying electronic devices. As an example, the newest electronic materials which host striking emergent quantum behavior are now constructed by making heterostructures out of single layers exfoliated from a host of layered materials [3]. This presents a challenge for STM measurements to use a tunneling probe to find and navigate to the device, since these heterostructured devices are small, on the tens of micron scale, and typically surrounded by insulating materials. Moreover, macroscopic electronic behavior in new materials is typically measured by magnetotransport, which complicates correlation with microscopic STM characterization if the measurements are not made on the same sample or in the same instrument. Therefore, the combination of AFM with STM and magnetotransport measurements at ultra-low temperatures can become a powerful platform for future quantum material research.

To meet these new challenges, we describe an instrument which allows simultaneous *in-operando* STM, AFM, and magnetotransport measurements while with an instrument possessing a resolving capability of sub 10 μeV in scanning tunneling spectroscopy (STS) operating at 10 mK. In this article we describe an extensive redesign of a previous mK STM system [10], which initially operated with a tunneling resolution equivalent to ≈ 230 mK. We incorporated in-situ cryogenic RF filtering, AFM and magnetotransport measurement capabilities, achieving a noise-limited resolving capability of ≤ 8 μeV. This resolution is close to the physical quantum and thermal limits at our operating temperature of ≈10-15 mK, determined from thermometry calibration [10]. The enhancements made to achieve a low-noise combined multi-mode instrument include: a redesigned and built SPM module with multiple contacts for sample and probe tips described in section II, RF filtering and cryogenic preamps for STM and AFM described in section III, AFM measurement capability described in section IV, magnetotransport capability described in section V. SIS tunneling measurements to characterize and optimize noise contributions and to determine the tunneling resolution are described in section VI, and a summary and conclusions are presented in section VII.

Certain commercial equipment, instruments, or materials are identified in this paper in order to adequately specify the experimental procedure. Such identification is not intended to imply recommendation or endorsement by the National Institute of Standards and Technology, nor is it intended to imply that the materials or equipment identified are necessarily the best available for the purpose.

II. A Multi-Mode SPM Module for STM, AFM, and Transport Measurements

A. Requirements for in-operando multi-mode measurements

1. Materials

The choice of materials for the SPM module are critical for multi-mode operation. The considerations include thermal management for cooling, thermal expansion, stiffness, and rigidity required to reduce mechanical vibration and achieve high quality factors *Q* for AFM measurements. In our initial version of this instrument we chose coin silver for the STM module, which satisfied most criteria except of thermal expansion [10]. With the module constructed from coin silver our *X-Y* coarse motion stage would sometimes freeze up or move with much reduced gain after cooling to low temperature. To overcome this limitation we switched to molybdenum for all module components which served well for our previous 4 K instrument [28]. The only exception was the bottom electrical plug which makes contact to the dilution refrigerator (DR): it was kept as coin silver for good thermal contact to the silver receptacle in the DR. An exploded model view of the STM module is shown in Fig. 1, and in the photo in Fig. 2. The module houses a *Z*-walker coarse motor stage with ±5 mm motion, which contains the *X-Y-Z* fine tube scanner along with the sample stage. An *X-Y* coarse motor stage with ±1.5 mm travel containing the tip stage is positioned above the *Z*-walker stage. All motor stages use Pan style [29,30] shear-piezo motors consisting of a stack of four shear-piezo sheets with copper electrodes [31] and an alumina cap epoxied together. Finally, on top of the SPM module is a locking stage containing a large compression spring used to press and lock the SPM module in the DR receptacle, as described previously [10].

2. Multi-contact sample and probe stages

Sample and probe tip stages comprise the heart of a SPM module and their designs are critical to a well-functioning system. They must incorporate the ability to utilize different sample geometries ranging from pure metal crystals to complex electrical devices with multiple electrical contacts. It is beneficial to have a kinematic mounting scheme so that the sample/probe is positioned in the same location within a few microns. More importantly, the mounts should allow for an easy and reliable insertion into the SPM module. Their design must also be compatible with the UHV transfer mechanisms used in the rest of the UHV systems and withstand the annealing procedures required for sample preparation. Poorly designed or malfunctioning sample/probe stages can lead to mechanical noise issues and unsatisfactory productivity of the instrument. To this end we completely redesigned the sample and probe tip systems carefully considering all engineering detail to meet the challenges indicated above. The redesign of the SPM module utilizes an eight-contact sample/tip stage with frictionless transfer (Fig. 3). To achieve the goal of multi-mode measurements, the SPM module had to accommodate at least 7-8 electrical contacts on the sample stage required, for example, for electrical measurements in quantum Hall devices, which typically would have at least six leads plus a back-gate wire. On the probe stage, the AFM/STM system required at least four contacts; two for the AFM signal, one for the STM tunnel current signal, and one for the electrical excitation of the qPlus sensor. We therefore chose eight electrical contacts for both the sample and probe tip systems, making them identical so they can share parts, and even be interchanged if desired. The electrical contacts consist of custom-made gold-plated beryllium-copper finger springs, which are glued into receptacles for the sample and probe tips (Fig. 3). The receptacles were engineered for a frictionless loading of sample and probe holders following designs developed in the group of H. J. Hug. The receptacle main body is made from molybdenum and has a three-point kinematic mount using three ruby balls glued into the receptacles which mate to 90° v-grooves in the sample/tip holder plates. The sample/tip holders, also made from molybdenum, are constrained in the receptacles using a beryllium-copper clamp spring which is actuated upwards by turning a screw in the receptacles using an Allen key wrench at the end of a wobble stick [Figs. 3(a) and 3(b)] [32]. This allows for the insertion of the sample and probe holders into the receptacles to be friction free with the spring not actuated in the down position during transfer, thereby avoiding the generation of wear particles, or breaking scanner piezo tubes or ceramics, which we have experienced with previous spring-loaded sample receptacles. The small threaded housing of the new receptacle is made from silicon bronze, while the screw is made from a tungsten alloy with Dicronite® coating [33], to achieve a smooth screw action with minimal force on the scanner, even at cryogenic temperatures. The sample and probe tip holders consist of a base plate made from molybdenum with three sets of 90° v-grooves. A metal or ceramic insert is inserted inside the base plate depending on the type of sample, or type of probe being used. An alumina insert with eight electrical contacts is inserted for device samples or probes, as shown in Figs. 3(b) and 3(c). Metal inserts were fabricated for pure metallic samples, which undergo high temperature annealing and sputtering. Using the Allen driver integral to the wobble stick to turn the receptacle screw activates the clamp spring and allows the sample/tip holders to make a stiff press contact between electrical pads on sample/probe alumina insulator inserts with the beryllium-copper finger springs, as shown in the photo in Figs. 4(a) and 4(b).

All instruments in the multiple UHV chambers and vacuum transfer systems were modified to accommodate the new sample and probe tips in the system [10]. To transfer the sample and probes throughout the vacuum systems, we designed a custom transfer receptacle [Fig. 4(b)]. This was built from a copy of the receptacles in the SPM module, but fabricated out of aluminum. Thus, this receptacle has the same frictionless transfer as in the SPM module and can accept any type of sample or probe tip used in the measurement systems. In addition, the transfer receptacle was designed and fabricated to connect all contacts of a device to ground through 1 MΩ surface mount resistors located at the top of receptacle housing [Fig. 4(b)]. For sensitive devices this avoids surge currents from the buildup of static electrical charges while transferring the device throughout the vacuum chambers. The aluminum transfer receptacles are screwed to baseplates, which were modeled after the typical flag style plates with three ball and spring friction receptacle mounts [34]. The transfer of the samples and probes is accomplished on flag base plates, while inserting them in spring friction mounts located on the various transfer stations (not shown).

3. X-Y capacitive position sensor

A position sensor is a very useful tool for navigating to a small device geometry as it can give an accurate description of relative motion during *X-Y* positioning using the *X-Y* coarse motion stage in a SPM. We implemented a design for a two-dimensional capacitive sensor based on Ref. [35] using a four-quadrant base electrode (4.3 mm × 4.3 mm) positioned about 75 μm from a 5.6 mm × 5.6 mm moving electrode, as shown in Fig. 5. The moving electrode is attached to a platform which is screwed into the tip receptacle [Fig. 3(c)], which moves in the *X-Y* plane as the *X-Y* motion stage moves the tip. The operating principle of the design is such that the four quadrants are fed AC signals that are phase shifted 90° with respect to each other. A lock-in amplifier measures the current to the moving electrode and thus both the *X* and *Y* positions of the sensor can be simultaneously read off the lock-in amplifier using the in-phase and out-of-phase components, respectively. The gap *d* between the base and moving electrodes determines the sensitivity of the position sensor, which can be seen from an analysis of the generated current into the moveable electrode from the *j*th base electrode given by $I_j = i\omega C_j V$, where ω and $V = V_0 \exp\,(i\varphi_j)$ are the excitation frequency and complex voltage, and C_j is the capacitance between the *j*th base electrode and the moveable electrode. The current simplifies to the following with 90° phase differences between the base electrodes,

$$I = 2\sqrt{2}l\left(\frac{\omega\epsilon_0 V_0}{d}\right)(X + iY). \tag{1}$$

The *X* position is directly proportional to the in-phase component and the *Y* position is given by the out-of-phase component. For our geometry the sensitivity is given by Eq. (1) to be 0.59 nA/μm of lateral motion with an excitation of 10 V amplitude at 10 kHz, which leads to submicron position sensitivity with measurements of the current at pA levels.

III. Pre-cooling, Wiring, RF Filtering, and Cryogenic Preamps for STM and AFM

A. Mechanical thermal switch for pre-cooling

One of the improvements we made in the DR was to change the pre-cooling system. The traditional method to initially cool a DR from room temperature is to leak a small amount of helium gas into the vacuum space to act as an exchange gas during initial cooling of the cryostat with liquid nitrogen, followed by liquid helium. The helium gas is then pumped out to high vacuum levels. However, a small film of liquid/solid helium will remain coating all the inner surfaces of the DR due to Van der Waals bonding even if pumped to UHV pressures. This will result in non-UHV operation and cause havoc with arcing and breakage of wiring in high voltage piezo motors. It will also contaminate surfaces with continued reabsorption of the released helium gas onto cold samples. This problem was solved in the original design of the DR [10], which used a capillary system connected to each stage of the DR. The capillaries went out to the top of the DR flange and could be filled with liquid nitrogen and helium during initial cool down. The system was functional but cumbersome to use because it required high pressure to force the liquid in the small diameter capillaries and it was inefficient. In addition, one had to take care to pump all the helium out of the capillaries at completion to avoid a thermal short between the DR stages; in the end we had to keep a small ion pump connected to this system after pumping for this reason.

To improve the efficiency and versatility of the pre-cooling system we replaced the capillary system with an all mechanical thermal switch (Fig. 6). The thermal switch consists of a gold-plated copper rod and compression spring attached to each stage of the DR. A stainless tube connected to a linear motion feedthrough on top of the main DR flange is actuated and presses the first rod/compression spring on the inner vacuum can (IVC) flange at 4 K. This then makes contact to the next rod/compression spring on the 1K pot, which then cascades to make a mechanical and thermal connection to each stage of the DR, stopping at the mixing chamber (MC) plate. The first rod at the IVC flange is connected via copper braids to a copper feedthrough on a mini-conflat flange on the IVC flange, which extends into the cryogen bath space, allowing efficient and easy cooling to each stage of the DR. This system is not only used during initial cooling of the DR from room temperature, but also each time the SPM module is lowered into the DR with a new sample. The MC temperature will rise to ≈ 60 K when the room temperature module is lowered into the DR at 4 K. Activating the thermal switch allows the DR to cool back to 4 K in less than 12 hours, typically overnight after loading the module. Our routine procedure is to warm up the DR to 60-80 K the day before using the SPM module to outgas the DR from any adsorbed background hydrogen, which is typically present in such a cryo-pumped system. The mechanical thermal switch has been improved in a more sophisticated design incorporating both rotating shutters [10] with the linear mechanical thermal switch on one feedthrough [36], thereby reducing the number of ports needed going into the DR space.

B. Dilution refrigerator wiring

To improve noise performance, the DR experimental wiring was replaced with new wiring since new connectors were needed for the RF filters on the MC plate. We used single flexible superconducting coax from room temperature to the mixing chamber made with a niobium-titanium core wire with Cu-Ni cladding and stainless steel outer braid separated by a Teflon dielectric [37]. Heat sinking was achieved with simple press Cu plates at each cooling stage of the DR (Fig. 6). We kept in place the original gold-coated Cu coax from the mixing chamber to the bottom of the STM mount, but changed connectors to sub-miniature push-on (SMP) [38] to attach to new RF powder filters, which contained integral SMP connectors on both ends, as described in the next section.

C. RF powder filters

Cryogenic RF filtering is commonplace in ultra-low temperature electrical transport measurements to reduce electrical interference over a broad range of frequencies and is used in sensitive experiments, e.g. to limit decoherence in qubit studies. In contrast, SPM instruments have used RF filters outside the vacuum chamber at room temperature, but it has been uncommon to find them in the cryogenic environment. The most popular cryogenic RF filter is based on small metal powders embedded in an epoxy matrix [23,39–42]. For our redesign we modified the design in Ref. [23] to incorporate RF powder filters on the mixing chamber, and also on the 4 K IVC flange (Fig. 6). We made two types of powder filters, a plain version with just a coil with a core of the metal powder in an epoxy matrix [Fig. 7(b)], and a π-version with two discoidal capacitors [43] at each end of the filter [Fig. 7(c)]. Each filter has SMP connectors [38] on both ends for convenient connections to cables at the MC plate [Fig. 7(e)]. The main housing of the filters has a ¼-28 threaded end and is screwed to the MC plate with good thermal anchoring [Fig. 7(e)]. We used the π-version on all low-voltage and piezo scanner signal lines, and the plain version on high voltage lines of the piezo motors. This choice was made due to possible voltage limitations of the discoidal capacitors at low temperatures, even though they are rated to 500 V at room temperature.

Figure 7 shows the various stages of construction of the powder filters. The central rod is cast from an epoxy-bronze powder solution following closely the optimum recipe in Ref. [42]. The epoxy mixture is, by weight, 80% Stycast 2850FT with catalyst 23LV, and 20% Stycast 1266, the latter reducing the viscosity for better incorporation of the metal powder and flowing into the filters housings. The bronze powder is composed of 80% copper and 20% tin with a particle size of ≈50 μm [44]. The epoxies are vacuum degassed before combining with the metal powder and subsequently vacuum degassed again after mixing to remove as many bubbles as possible. The mixture is put into Teflon blocks with a lattice of holes with the diameter set for the central rod. After curing the rods are trimmed and side and axial holes are drilled at each end. A 0.10 mm Kapton®-coated wire is wound tightly around the rod and passed through the end holes of the rod [Fig. 7(a)]. Discoidal capacitors and SMP connectors are then attached to the ends of central rod for the π-version [Fig. 7(d)] or simply SMP connectors for the plain version [Fig. 7(b)]. Finally, the central rods are potted into bronze cylinders with additional epoxy-powder emulsion and cured [Fig. 7(c)]. The finished filters are screwed into a Cu plate attached to the mixing chamber [Fig. 7(e)].

Transmission characteristics of the two types of filters, measured at room temperature, are shown in Fig. 8. Both types of filters start to show attenuation above about 2 MHz. The plain version shows a gradual decrease in attenuation reaching about -13 dB at 10 MHz and -50 dB at 2 GHz. In contrast, the π-version of the filter shows a sharp attenuation beginning at 2 MHz and reaching -45 dB at 10 MHz, and the noise floor of the analyzer at around 100 MHz. Both types of filters show characteristic high frequency resonances of this design [23]. We specifically built the plain filter for low capacitance with an increased spacing from the wound inner rod to the shell of the filter to allow use in the tunneling current signal line. Additional powder filters are placed on the 4 K IVC flange to filter the incoming lines going to the cryogenic preamp (Fig. 6).

D. Cryogenic preamps for STM and AFM

Cryogenic preamps help reduce the noise contributions in STM and AFM measurements due to several factors including: reduced Johnson noise from large transimpedance gain resistors, reduced power-line pickup, reduced triboelectric pickup, and most importantly reduced cable capacitance due to shorter cables since the cryo-preamps are placed close to the microscopes [45]. Cable capacitance is particularly important for quartz type tuning fork sensors, such as the qPlus force sensor [46]. To this end we used a specially designed low capacitance cable. For a coax cable with inner wire of radius a, and outer shield of radius b, the capacitance per unit length is given by

$$\frac{C}{L} = \frac{2\pi\epsilon\varepsilon_0}{\ln\left(\frac{b}{a}\right)}, \tag{2}$$

where ϵ is the dielectric constant, L is the cable length, and ε_0 is the permittivity of free space. We therefore chose the inner conductor to be as small as possible and practicable to minimize a, with a thick dielectric to maximize b in Eq. (2). The cable we had fabricated was made from twisted pair 0.05 mm diameter niobium-titanium core with Cu-Ni cladding (for good soldering purposes) and 0.25 mm thick Teflon dielectric with a low-noise coating. A stainless-steel braid with 0.05 mm diameter wires with a 0.127 mm thick second outer Teflon jacket covered the twisted cable (twinax cable) [37]. The measured capacitance values are 18 pF/m between the twisted cables, and 47 pF/m between twisted pairs and outer shield; the latter value agreeing with the simple formula estimate in Eq. (2).

The preamp is based on the floating design in Ref. [7], which is used here to float both the STM and AFM preamps at the tunneling bias potential, shown in Fig. 9. The STM component is a simple transimpedance amplifier, and the specific AFM core design is a differential amplifier based on Ref. [47]. In this design, both the AFM and STM preamps commons are at the tunneling bias voltage which has its ground referenced (cold reference) from the SPM module body through a buffer amplifier. This design tends to cancel ground fluctuations between the cold junction and upper room temperature electronics. A conditioned version of the bias voltage is then used as a reference voltage and to drive the preamp housing and shields of the twinax cables for the STM and AFM input signals, further reducing the parasitic effects of the shield-to-core input capacitance.

The cryo-preamps were constructed on a ceramic circuit board enclosed in a set of nested boxes (Fig. 10). The op amps [48] are lifted off the circuit board with 2 mil stainless wires to allow the op amps to self-heat to a stable operating temperature without requiring an additional heater. The cryo-preamps can be started when the cryostat is operating at base temperature and do not need to be kept operational during cooldown. The inner box is driven at the guard voltage reference providing a complete homogenous floating circuit reference for the circuit board and STM and AFM input cable shields. The inner box is electrically isolated from an outer box which is bolted to the IVC flange at 4 K (Fig. 6).

The performances of the cryo-preamps are shown in Fig. 11 and Fig. 12 for the AFM and STM preamps, respectively. The AFM preamp spectral noise density in Fig. 11 is at a value of $n_{el} \approx 1.5\ \mu\mathrm{V}/\sqrt{\mathrm{Hz}}$ near the qPlus sensor operating frequency of ≈23 kHz. This value determines the force noise as described in a more detailed analysis of the AFM performance presented in Section (IV.B). The STM preamp current noise spectral density shown in Fig. 12 is less than 6 $\mathrm{fA}/\sqrt{\mathrm{Hz}}$ at 600 Hz and shows very low noise peaks at power line harmonics, which is both difficult to achieve with long cables to external preamps and distributed grounds. Although the low frequency performance of the output signal is very good, it does not tell us about high frequency noise contributions which may be present on the input and thus affect the ultimate energy resolution. This will require extensive measurements using Josephson tunneling as discussed in Section (VI) and will show this internal preamp is not the best choice for ultimate energy resolution in tunneling spectroscopy. In addition to the cryogenic preamps, we designed the system so that an external STM preamp could be used, as shown in the circuit diagram in Fig. 9. To select between internal vs. external preamps, is just a matter of wiring the probe tip to a different electrical contact on the tip holder. This allows different current gains to be used with an external preamp, and, as shown in Section (VI.B), various preamps affect the tunneling energy resolution in different ways. We speculate this may be due to having a RF powder filter on the input cable to the external preamp, which we did not include on the internal preamp input cable. Further modifications and testing is required to check this hypothesis.

IV. Adding AFM Measurement Capability

A. A qPlus sensor for mK systems

We chose to add AFM capability based on the qPlus sensor [49] to the SPM system as it is the easiest to integrate into a dilution refrigerator, or any STM system for that matter, and allows for simultaneous AFM and STM measurements. The qPlus sensor consists of a specialized quartz tuning fork with one prong fabricated with a large mass substrate, resulting in a single oscillating quartz beam. The three dominant noise sources which contribute to the frequency shift measurements are thermal noise, oscillator noise, and detector noise [50,51]. The three noise sources add in quadrature, where thermal noise and oscillator noise have a constant noise density ("white noise") and the detector noise density rises linearly with modulation frequency ("blue noise"). For typical scanning speeds, detector noise is typically the dominant noise source and is greatly influenced by the input cable capacitance [47]. To reduce cable capacitance, it is therefore desirable to place the preamp as close to the sensor as possible with the shortest input cable length. The challenge for a mK SPM system is that the preamp cannot be placed as close to the qPlus sensor as in 4 K systems. For the mK system, the closest we could place the preamp is at the 4 K

IVC flange, ≈1050 mm distance from the bottom of the SPM module, as compared to 25-50 mm for a 4 K system. We therefore designed a low capacitance cable for the preamp inputs using twisted pair construction as described above. Furthermore, for this mK system a new qPlus sensor was designed with an additional electrode for electrical excitation, thereby eliminating the need for a shaker piezo. This allowed for a more rigid probe holder and sensor combination. The resulting sensor has four contacts, two for the electrical readout of the quartz sensor (AFM1 and AFM2), one for the electrical connection to the tip (STM), and one for the electrical excitation (Excitation), as shown in Fig. 13. A custom "T" insert made from molybdenum is used to mount the sensor symmetrically at the probe holder, as shown in Fig. 14. The "T" insert is screwed to the probe holder plate and two quartz plates with predefined electrical pads are glued to the side faces of the "T" insert. One plate (the back one) has the electrode for the electrical excitation, and the front-facing plate in Fig. 14 shows three electrical contacts for the oscillation detection and the electrical tip connection. These electrical strips are then connected to the wire-bonding pads of the probe holder with thin gold wires.

After the tip holder plate with mounted sensor is transferred into the SPM module, its Q-value is measured at room temperature in the upper UHV chamber before transferring the SPM module into the DR/cryostat. We found it is important that the sensor is mounted tightly into the probe holder to enable a stiff mechanical connection. Fig. 15 shows the Q-value before and after tightening the connection between the tip holder plate and the tip receptacle, respectively, as measured at room temperature in the upper UHV chamber. After tightening and cooling to mK temperatures the Q-value rises to above 100k. In the next sections, we describe the noise characteristics and field dependence of the qPlus sensor operation at mK temperatures and in high magnetic fields. Using the sensor for imaging is described in section V.

B. Performance of mK qplus AFM

1. AFM Noise characteristics

As we are operating at lower temperature and higher magnetic fields (which affects the oscillator quality factor Q) than those achieved previously for AFM measurements, it is instructive to compare the various noise sources in the AFM measurement. To characterize the qPlus sensor performance we consider how each main noise source affects the precision of the AFM measurement for the mK SPM system. The main differences with previous instruments are the detector noise contribution from the cryo-preamps and thermal noise at mK temperatures. In frequency modulation AFM [50] the qPlus sensor is always excited at its resonance frequency and vibrates with a constant amplitude, A. Without any tip-sample interaction the resonance frequency is the unperturbed eigenfrequency f_0 of the sensor. When the sensor's tip interacts with a surface its resonance frequency changes from the unperturbed resonance frequency f_0 to $f_0 + \Delta f$ due to an acting force gradient, k_{ts}, between the sensor probe tip and sample. With the resonance frequency condition of the unperturbed sensor, $f_0 = \frac{1}{2\pi}\sqrt{k/m^*}$, the frequency shift is given by

$$\Delta f = \frac{f_0}{2k}\langle k_{ts}\rangle, \tag{3}$$

where $\langle k_{ts}\rangle$ is an average force gradient given by the integral of the tip-sample force gradient multiplied by a semicircular weight function, as a function of tip-sample distance [52]. It follows from Eq. (3) that the precision of the measurement of the force gradient is given by

$$\delta k_{ts} = 2k\frac{\delta f}{f_0} \tag{4}$$

with the precision of the frequency measurement δf. We now consider how the three main noise sources contribute to δk_{ts} for our mK SPM system: the detector noise, $\delta k_{ts\,det}$, the thermal noise, $\delta k_{ts\,th}$, and the oscillator noise, $\delta k_{ts\,osc}$. These add in quadrature to give the total noise in a measurement of the tip-sample force gradient as

$$\delta k_{ts\,sum} = \sqrt{\delta k_{ts\,det}^2 + \delta k_{ts\,tm}^2 + \delta k_{ts\,osc}^2}. \tag{5}$$

2. Deflection detector noise

For scanning speeds that require a detection bandwidth above about 30 Hz (see Fig. 18), the largest noise contribution arises from how precise we can measure the deflection of the cantilever because of the preamplifier detector noise. Any deflection noise density, n_q, in $\mathrm{m}/\sqrt{\mathrm{Hz}}$, will translate into a frequency noise given by [51]

$$\frac{\delta f}{f_0} = \sqrt{\frac{2}{3}}\frac{n_q B_W^{\frac{3}{2}}}{A f_0}, \tag{6}$$

where B_W is the bandwidth of the measurement. We evaluate the deflection noise density from the preamplifier noise density n_{el} considering how the qPlus sensor transduces voltage from deflection, which is given by its sensitivity factor, S_V, in $\mathrm{V/m}$. The deflection noise density is thus given by

$$n_q = \frac{n_{el}}{S_V}, \tag{7}$$

where n_{el} is preamplifier noise density described in Section (III.D), and S_V is determined from calibration measurements. From Fig. 11 we determine the preamplifier noise density near the resonance frequency to be $n_{el} = (1.44 \pm 0.01)\ \mu\mathrm{V}/\sqrt{\mathrm{Hz}}$. The sensitivity factor is obtained from the measurement of the tip equilibrium position versus oscillation amplitude in AFM feedback [53] at constant frequency shift Δf. From Fig. 16 we determine $S_V = (8.66 \pm 0.01)\ \mu\mathrm{V/pm}$ from a linear fit for oscillation amplitudes greater than 40 mV. The resulting deflection noise density from Eq. (7) using this sensitivity is then $n_q = (166.3 \pm 1.3)\ \mathrm{fm}/\sqrt{\mathrm{Hz}}$. As a check, the deflection noise density can also be estimated from the measurement of frequency shift noise density vs modulation frequency, by measuring the spectral density of the frequency output with a spectrum analyzer (Fig. 17) [47]. The low-frequency regime of the frequency shift noise density is linear in modulation frequency and proportional to n_q up to the bandwidth of the measurement [54]. A linear fit to the low frequency region from 10 Hz to 150 Hz yields $n_q = (170.1 \pm 1.4)\ \mathrm{fm}/\sqrt{\mathrm{Hz}}$. Taking the average of these two methods thus yields a final value for the deflection noise density of $n_q = (168.2 \pm 1.9)\ \mathrm{fm}/\sqrt{\mathrm{Hz}}$ for our mK system. The deflection noise density is about seven times larger than the noise density obtained with the same preamp, but with short cables (see Table 1). This shows the cable capacitance is the dominant contribution to the increased deflection noise reflected in the increased preamplifier noise density by a factor of almost ten, $n_{el} = (1.44 \pm 0.01)\ \mu\mathrm{V}/\sqrt{\mathrm{Hz}}$ for our mK system compared to $n_{el} = (0.136 \pm 0.006)\ \mu\mathrm{V}/\sqrt{\mathrm{Hz}}$ obtained with short cables in a 4 K system [47].

We now can arrive at our detector noise with Eqs. (4) and (6) and the value of n_q above; $\delta k_{ts\,det} = (10.4 \pm 0.1)\ \mathrm{mN/m}$ for the parameters $A = 50$ pm, $f_0 = 30$ kHz, $k = 1800$ N/m, and $B_W = 10$ Hz. This value is approximately seven times larger than for short-cabled 4 K systems (Table 1), since the noise scales directly with n_q [Eq. (6)], and we found n_q was seven times larger for our system. However, a force gradient noise comparable to the best obtained measurements of $\delta k_{ts\,det} = 1.5\ \mathrm{mN/m}$ at $B_W = 10$ Hz (see Table 1) can be obtained in our longer cabled system using a bandwidth which is about 3.6 times smaller since $\delta k_{ts\,det}$ scales as $B_W^{\frac{3}{2}}$. For example, $\delta k_{ts\,det} = (1.3 \pm 0.02)\ \mathrm{mN/m}$ at $B_W = 2.5$ Hz.

3. Thermal and oscillator noise

The two other noise contributions to the AFM measurements are the thermal noise and oscillator noise. The thermal noise is given by [50]

$$\delta k_{ts\,th} = \sqrt{\frac{4kk_B T B_W}{\pi A^2 f_0 Q}}\,, \tag{8}$$

where k_B is the Boltzmann constant, T is the temperature, and Q is the quality factor, and similarly the oscillator noise is given by [51]

$$\delta k_{ts\,osc} = \sqrt{2}\frac{kn_q}{AQ}\sqrt{B_W}. \tag{9}$$

Figure 18 compares these three noise figures and their total sum [Eq. (5)] versus Q-value. The thermal noise contribution from Eq. (8) has the smallest contribution for all reasonable Q values given an operating temperature of 15 mK. In addition, Fig. 18 shows that detector noise dominates for values of $Q > 1 \times 10^4$, even for low bandwidth measurements. Thus, we are able to achieve atomic resolution with AFM feedback and resolve interesting quantum states in frequency shift measurements on gated graphene devices with our qPlus AFM operating at mK temperatures and in high magnetic fields, as described in upcoming sections.

4. Magnetic field dependence

The use of qPlus sensors in high magnetic fields is relatively new, and the dependence of the sensor characteristics vs. magnetic field strength need to be determined. Recent measurements of generic tuning forks have shown an inverse of the damping constants to scale with the square of the magnetic field due to eddy current damping in the leads causing dissipation [55]. As the quality factor is proportional to the relaxation time, we expect a similar relationship should hold for the inverse of quality factor versus magnetic field.

Figure 19(a) shows the resonance peak for magnetic fields, *B*, between 0 T and 7 T showing a decrease in amplitude and shift to higher frequency with increasing magnetic field. The center frequency shows an approximately linear relationship with field [Fig. 19(b)], while the quality factor, Q, decreases gradually from over 10^5 at zero field to $\approx 2 \times 10^4$ at 7 T [Fig. 19(c)]. At the highest magnetic field of our system of 15 T, the quality factor Q reduced to $\approx 5 \times 10^3$. Figure 19(d) shows that inverse of the quality factor scales with square of the magnetic field with slope $(9.52 \pm 0.09) \times 10^{-7}\ \mathrm{T}^{-2}$. This is similar as reported for generic tuning forks suggesting eddy current damping due to the sensor electrodes causing dissipation. Reducing the amount of electrode material or changing to more resistive materials may reduce this effect. However, Fig. 18 shows that the detector noise is still the dominant contribution to frequency shift noise for quality factors $\mathrm{Q} > 1 \times 10^4$, and large values of magnetic field are not detrimental to obtaining high quality AFM measurements.

5. *Imaging with the mK AFM*

With the qPlus sensor we are able to obtain both AFM and STM signals simultaneously with atomic resolution. We show this using an iridium tip (0.05 mm diameter) and a ≈ 100 nm thick grown aluminum sample (Fig. 20). Figure 20 shows the topography [Fig. 20(a)] and tunneling current [Fig. 20(b)] images of the aluminum film recorded in AFM feedback, with a frequency shift setpoint of -3.5 Hz, an oscillation amplitude of 300 pm, and a sample bias of -18 mV. The aluminum films are used in SIS tunneling for evaluating the noise performance shown in Section (VI). A variety of defects are observed on the surface and their appearance is different in the two channels. Apparent protrusions in the topographic image (AFM image) appear dark in the current signal reflecting a reduced tunneling probability. Conversely, defects with little topographic variation (possibly in plane defects) appear bright in the STM channel. The topographic image recorded with a frequency shift setpoint of -33 Hz and an oscillation amplitude of 500 pm in Fig. 20(c) shows the atomic resolution capability at 10 mK, indicating the as-grown aluminum film is in the (111) orientation.

V. Adding Magnetotransport to an SPM System

Magnetotransport measurements are enabled in the SPM system through adding eight contacts to the sample holder and receptacle, as described in Section (II.A.2). Fig. 21(a) shows a microscope photo of a typical graphene device consisting of a single layer of graphene transferred onto hexagonal boron nitride (hBN) insulator which is exfoliated on a SiO_2/Si(p) substrate, also used for a back gate. Six electrical contacts, bonding pads, and a navigation runway are fabricated onto the device using e-beam lithography. The navigation runway is required to assist in finding the central device area and consists of gold steps, ≈50 nm in height, aiming towards the device center and fanning out to a dimension of $\approx 500\ \mu$m. The probe tip is aligned optically over the gold runway when the SPM module is in the upper SPM UHV chamber. The SPM module is then lowered and locked into the DR SPM receptacle. After cooling to base temperature, the probe alignment set optically at room temperature is typically preserved to within $\approx \pm 20\ \mu$m, due to the use of low thermal expansion materials such as molybdenum. A robotic navigation algorithm is used to navigate along the gold step ridge using STM or AFM feedback until the graphene area is found. Figures 21(b) shows a zoomed in photo of the Hall bar. The graphene area was shaped into the Hall bar geometry (grey area) using oxygen plasma reactive ion etching, thereby creating a physical graphene boundary. In AFM frequency shift measurements performed by scanning at constant height parallel to the average sample slope, we could easily distinguish between the conducting graphene and the insulating hBN with a strong contrast, as shown in Fig. 21(b) where four AFM images are shown overlaid on top of the graphene area. The AFM images (iii) and (iv) show the sample topography recorded with the frequency shift setpoint of –40 mHz using an oscillation amplitude of 2 nm. Zooming into the conducting graphene area allows STM measurements to be obtained with atomic resolution [Fig. 21(c)]. Another useful aspect of the AFM is using constant-height AFM imaging at (30-40) nm away from the surface to navigate the runway towards the central graphene device area [Fig. 21(a)]. This avoids wear and tear of the probe during fast large-image scanning.

Magnetotransport measurements are obtained with an AC current running through the source-drain outer contacts and measuring the longitudinal and transverse Hall resistance. Quantized conductance is observed for this device in Fig. 22, which shows the Hall conductance versus magnetic field up to 15 T. The Hall conductance shows some deviation from perfect behavior due to admixture of longitudinal conductance since the signal was measured diagonally across contacts, as one side contact opened during fabrication. Having combined measurements allows for a comparison of the macroscopic transport measurements with microscopic STS Landau level spectroscopy, which can be performed as a function of back gate, as shown in Fig. 23. Here we see a series of metal insulator transitions as the gate voltage is varied. Large diamonds appear in the gate map at the Fermi level at integer filling factors when the system undergoes a transition between different Landau levels, which can be correlated with the macroscopic magnetotransport measurements in Fig. 22. The STS measurements in Fig. 23 shows additional more complex local features (slanted lines in Fig. 23) related to Coulomb charging of quantum dots forming in the inhomogenous potential landscape [56,57]. Current research efforts are focused on measuring the electronic states in a quantum Hall device near the boundary edges with AFM and STM measurements [58]. Landau level spectroscopy can also be obtained with AFM Kelvin probe measurements, which monitors the change in chemical potential as Landau levels are filled or emptied [58]. The Kelvin probe measurements have the advantage of not inducing a charge carrier density bubble under the probe tip as it operates at zero contact potential difference.

VI. Benchmarking μeV Energy Resolution with Josephson Tunneling

The highlight of our efforts in this instrumentation development is the achievement of sub 10 μeV instrument resolving capability in tunneling spectroscopy. Prior to this development our STS resolution was noise limited and comparable to an ≈230 mK equivalent temperature, as shown in Fig. 24. This is significantly larger than the operating temperature of the dilution refrigerator of 10 mK. The effective temperature is not a good benchmark to describe the instrument response as it is a measure of a convolution of several factors including electrical noise, intrinsic temperature, and quantum broadening from the electromagnetic environment. In addition, the fits can vary depending on the specific models used to fit the spectra. A better way to examine the resolution is then to determine the amount of voltage noise contributing to the measured spectra in addition to thermal and quantum effects. From simply examining the slope of the coherence peak transitions in Fig. 24, one can estimate a noise contribution of ≈ 100 μV to the tunneling spectrum. A better estimate can be extracted from the temperature used to fit the spectrum in Fig. 24, which equates to Fermi-Dirac energy broadening, $\approx 3.5\ k_{\mathrm{B}}T = 69$ μV. Since this is much larger than the intrinsic thermal broadening of $3.5\ k_{\mathrm{B}}T = (3.0 - 4.5)$ μV at $T = (10 - 15)$ mK, the spectrum is certainly dominated by the electrical noise contribution of ≈ 70 μV. To reduce the electrical noise contributions to a negligible amount so the spectra are dominated by the apparatus temperature was one of the main goals of the current instrumentation development. To achieve this level of resolution we followed previous reports [16,59] and used SIS tunneling junctions as detectors of electrical noise. Below we describe the steps taken to examine every contribution to noise to the SIS tunneling spectrum. The advantage of the SIS measurement is that it is relatively insensitive to temperature below the critical temperature of the superconductors, and therefore deviation from ideal SIS spectra is largely due to noise contributions, until the quantum limit is reached [59]. Thus, a SIS junction makes an ideal noise meter.

The SIS devices were made using an ≈100 nm thick aluminum sample grown by molecular beam epitaxy onto graphene/SiC substrates, which can be transferred right after growth in UHV into the SPM module. For the probe we used a 0.8 mm diameter aluminum wire simply cut with cutting pliers. A typical spectrum of the SIS junction after all our efforts to reduce the electrical noise interference is shown in Fig. 25, where both the coherence peaks at gap energies of Δ and 2Δ, and Josephson peak at zero bias are seen. As shown below, the coherence peaks are not a good measure of resolution at this noise level. They are intrinsically limited by material parameters and a better measure of the resolution is obtained by zooming in on the Josephson tunneling peak at zero bias, as shown in Fig. 26. Figure 26(a) shows the $I(V)$ characteristics with a transition width of approximately $\approx$ 11 μV, which is also equivalent to the zero-crossing width of the differential conductance signal in Fig. 26(b). We denote the zero-crossing width in the *dI/dV* Josephson peak as Γ_{Zero}. Another measure of the instrument resolving function is given by examining the full-width-half-maximum of the peak (Γ_{FWHM}) in Fig. 26(b) which is $\approx$ 7.6 μV. We point out that the width of the Josephson peak in the *dI/dV* spectra in Fig. 26(b) is not a measure of the tunneling energy resolution in this specific measurement. Γ_{FWHM} underestimates the energy resolution in the measurement as it involves a difference of $P(E)$ functions related to the electromagnetic environment (see Section VI.D and Ref. [59]), but presents a well-comparable benchmark of the resolving power of the instrument in tunneling spectroscopy. We discuss further the energy resolution functions in Section VI.D. In the following sections, we first detail the various sources of noise which are seen by using the SIS junction as a noise detector.

A. Dependence on Tunneling Impedance

The ideal superconducting tunneling spectrum has infinitely large coherence peaks due to the divergence at energies equal to the energy gap, or twice the gap for SIS tunneling. These infinities are broadened by noise contributions, intrinsic parameters due to orbital depairing and spin-orbit scattering [60,61], and higher order tunneling processes [62]. At the lower noise level we have currently achieved, the coherence peaks can be intrinsically limited and are no longer dominated by noise. This can be seen in the dependence on junction impedance, which is shown in Fig. 27. In Fig. 27(a) the coherence peaks decrease in intensity as the junction impedance is lowered. Zooming in on the negative bias peak in Fig. 27(b) shows the decrease in amplitude is also followed by an increase in the width of the coherence peak. This shows that the coherence peaks themselves are no longer a good measure of noise contributions with our current noise limit, but are limited by intrinsic processes, such as higher order tunneling processes [62] and possibly by orbital depairing and spin-orbit scattering depending on material parameters. The latter can be extracted from a fit to the Maki tunneling theory, which we describe in Section (VI.D).

B. Dependence on Transimpedance Amplifier

Somewhat unexpectedly to us, the choice of transimpedance amplifier significantly contributed to the apparent junction noise. Although the cryogenic STM preamplifier showed good noise performance at low frequency in Fig. 12, it contributed an excess of electrical noise to the tunnel junction resulting in an equivalent noise level of $\approx 100\ \mu$V. We therefore obtain our best resolution with an external STM preamplifier, which can be selected instead of the internal one by wiring the probe tip to different electrical contacts on the probe holder, as described in Section

(II.A.2). We speculate one source of the excessive electrical noise with the internal preamp is caused by the lack of an RF power filter in the input line of the preamp (see Fig. 9). Therefore, all the following measurements are made with an external STM preamp. AFM measurements, however, use only the cryogenic preamp described in Section (III.D).

Figure 28 shows SIS tunneling measurements using three different commercial transimpedance amplifiers. One can see that preamp “A”, NF SA-606F2 [63], gives the largest coherence peaks, followed by preamp “B”, FEMTO DLPCS-100 [64], and then “C”, DL 1211 [65]. Although a change in the coherence peak height is clearly detectable with the different preamps [Fig. 28(b)], the Josephson tunneling gives a much more surprising differentiation, as shown in Fig. 28(c). Here we see a dramatic difference in noise contributions between the various preamps with preamp “A” [63] resulting in a Josephson zero bias peak with $\Gamma_{FWHM} \approx 7.9\ \mu$V. Preamps “B” [61] and “C” [65] yield a much-broadened peak of three to four times that of preamp “A” such that the oscillations in the tunneling spectra near zero bias are not clearly resolved. All further measurements, illustrating the influence of different components in the setup including the previous discussion of the impedance dependence in Fig. 27, therefore, are shown using only preamp “A” [63].

C. Dependence on External Filters, Grounding, and Signal Sources

The grounding scheme is also important. The cryostat is made the low-noise ground point of a “star” circuit. The cryostat is electrically isolated from the UHV chambers using a ceramic break. It is connected to the low-noise ground available in the laboratory. Therefore, no other signals should carry a ground to the cryostat. To achieve this, we use differential amplifiers on all signals going into and coming out of the cryostat (Fig. 9).

For our measurement system we use the Nanonis BP5 control system with the SC5 signal conversion module and high-voltage amplifier, together with the OC4 oscillation controller for AFM [66]. Attention to the grounding and filtering of these signals is paramount to achieve low-noise STS measurements. We feed the tunnel bias signal to the UHV chamber via a battery powered conditioning circuit, with an instrumentation amplifier [67], a passive attenuation stage and an active low-pass filter stage with a low-noise operational amplifier [68]. The gain of the attenuation stage can be chosen between $\times 1$ and $\times 0.001$, depending on the voltage range or resolution required for the experiment. The low-pass filter cutoff frequency can be selected between 20 kHz, 5 kHz, 3 kHz and 1kHz. The settings used for the following measurements are an attenuation of 0.001 and low pass filter of 1 kHz. Conditioning the tunnel bias signal in this way ensures it is free of ground loops, power-line and common mode noise, as well as of any high-frequency noise components present in the Nanonis signal outputs. We found, however, that further passive low-pass filtering is required to achieve a maximum reduction in noise in STS measurements. Therefore, we tested various RF filters, which are summarized in Fig. 29. The worst case, "E" results in $\Gamma_{Zero} \approx 53$ µV, $\Gamma_{FWHM} \approx 35$ μV when no filter is used. A very small improvement is made in case "D" using a 1.9 MHz RF filter [69] with $\Gamma_{Zero} \approx 45$ µV, $\Gamma_{FWHM} \approx 28$ µV. A noticeable improvement is made in case "C" using a 1 kΩ resistor on the input before the chamber as part of a × ½ voltage divider (see Fig. 9). This forms a 36 kHz low pass filter with the 4.4 nF capacitors in the π-power filter on the bias input (see Fig. 9). A slightly better reduction is observed in case "B" with a commercial high grade 50 kHz low-pass RF filter [70], together with the 1.9 MHz RF filter. Finally, the best performance is to use all three filters, the voltage divider together with the 1.9 MHz RF filter and the 50 kHz RF filter, resulting in a $\Gamma_{Zero} \approx 10.6$ µV, $\Gamma_{FWHM} \approx 7.8$ µV. This is the final configuration we settled on for our measurement system. No other changes have decreased the noise any further indicating this may be the resolution given by our operating temperature.

Other signals which need attention are the high-voltage scanner and piezo-motor signals. While the reference for all low-voltage signals is brought to the cryostat ground by the means of instrumentation amplifiers, the high-voltage scanner signals preclude this approach. In this case care needs to be taken of the cabling of the Nanonis high-voltage power supply. There are two grounds available on the unit, the chassis ground, connected to protection earth (PE), and the high-voltage (HV) circuit ground. We utilize an isolation transformer [71], with the PE of the secondary side grounded to the cryostat ground, connecting the PE of the Nanonis high-voltage power supply as well as the DC power supply of the external STM preamplifier to this ground. For the Nanonis high-voltage amplifier, we made a custom cable which connects the HV circuit ground to the cryostat for each HV signal, cf. figure 17 in Nanonis HVA4 high-voltage amplifier manual [66]. The signals are filtered at the UHV chamber with a D-Sub RF filter adapter [72]. We verified these signals are not contributing significantly to the noise level as there is hardly any change in the spectral width with a change in HV gain in the range from $\times 4$ to $\times 15$; if the HV signals were contributing significantly there would be a dependence on HV gain. Note that the digital interface cable for controlling the high-voltage gain of the Nanonis high-voltage amplifier usually connects the chassis grounds of the control unit and the amplifier. Since the cable is not required during measurements, it is therefore removed from our setup after the gains are selected.

One signal connection which could not be filtered and had a deleterious effect on the tunnel spectrum was one of the piezo-motor signals. We did not filter these at room temperature since these operate at very high voltages and we did not want to slow down the sharp transient which is needed for stick-slip motion. We did implement plain powder filters for all these signals on the mixing chamber, however. In spite of the powder filter, the noise level is so large that no Josephson peak can be observed with the piezo-motor signal cable connected to the cryostat as the noise completely broadens it out. The large noise contribution can be observed examining one of the coherence peaks in the tunneling spectrum, as shown in Fig. 30. One can see the coherence peak is broadened by ≈ 200 μV compared to when the piezo motor is grounded to the cryostat and disconnected from the Nanonis system. This larger noise contribution is likely due to the high bandwidth requirements of the piezo-motor controller required for the very fast voltage transients for piezo motor stick-slip actuation. For this reason, we only connect the piezo-motor cable when coarse tip-sample positioning is needed, then for high-resolution measurements we disconnect the cable and short all piezo-motor signals to the cryostat ground.

Another ground related noise source we encountered was from the heaters on the resistance bridge which reads the RuO thermometers [73]. There are two heaters, one for the mixing chamber and one for the STILL. These two heaters have different grounds in the bridge circuitry. One of them is optically isolated and can be used to directly connect to the mixing chamber heater. The other heater used for the STILL has its connections referenced to chassis ground, which we found added noise to the measurement. Therefore, we set up a differential amplifier to receive the STILL heater signal and break the ground path before going to the heater in the DR. The analog common of the optically decoupled AC measurement frontend is connected to the cryostat ground. One final check was made is to see if reading the temperature sensors contributed to any noise. We verified that they do not; no change in spectra was observed with the temperature sensors connected and reading with the resistance bridge [73].

D. Analysis of SIS Spectra and Ultimate Energy Resolution

In this section, we discuss the analysis of the observed energy resolution in the context of the $P(E)$-theory which accounts for coupling of the tunneling electrons to the electromagnetic environment. Reference [59] gives a thorough description of how the capacitance of the tunnel junction contributes to the tunneling energy resolution at ultra-low temperatures. Here we summarize the main points of the $P(E)$-theory which describes the probability of tunneling electrons to exchange energy with the electromagnetic environment.

To account for the coupling of the tunneling electrons to photons in the surrounding environment the standard tunneling probability for tunneling from tip to sample is modified by a convolution with the $P(E)$ function as

$$\vec{\Gamma}(V) = \frac{1}{e^2 R_\mathrm{T}} \int_{-\infty}^{\infty} \int_{-\infty}^{\infty} dE dE' \, n_t(E) n_s(E' + eV) f(E)[1 - f(E' + eV)] P(E' - E)\,, \qquad (10)$$

where R_T is the tunneling resistance, $f(E) = 1/(1 + \exp(\mathrm{E}/k_\mathrm{B}\, T))$ the Fermi function, and n_t and n_s are the tip and sample density of states, respectively. The reverse probability for tunneling from sample to tip, $\overleftarrow{\Gamma}(V)$ is given by exchanging electrons with holes and the total tunneling current is given by the difference between $\vec{\Gamma}(V)$ and $\overleftarrow{\Gamma}(V)$. From Eq. (10) we see that in addition to the thermal broadening by the Fermi distribution we have an additional broadening by the $P(E)$ distribution, so that in the limit of ultra-low temperatures and low extrinsic noise the tunneling spectra is dominated by the broadening by $P(E)$. The measurements shown above are near this limit, which can be seen by examining both the contributions from thermal broadening and $P(E)$.

The $P(E)$ function describing the coupling to the environment can be conveniently broken into two terms, as shown in Ref. [59] as

$$P(E) = P_0(E) * P_{\mathrm{N}}(E) = \int_{-\infty}^{+\infty} dE'\, P_0(E - E')P_{\mathrm{N}}(E'), \tag{11}$$

where P_0 describes the environmental impedance and P_{N} describes the capacitive noise. The function P_{N} can be modeled as a simple gaussian to account for the thermal capacitance noise as

$$P_{\mathrm{N}}(E) = \frac{1}{\sqrt{4\pi E_{\mathrm{C}} k_{\mathrm{B}}\, T}} \exp\left[-\frac{E^2}{4E_{\mathrm{C}} k_{\mathrm{B}}\, T}\right], \tag{12}$$

where the charging energy $E_{\mathrm{C}} = Q^2/2C_j$ and C_j is the junction capacitance. One sees that the width of $P_{\mathrm{N}}(E)$ is determined by the ratio of T/C_j. The distribution will become narrower for lower temperatures and large junction capacitances. Examples of spectra showing a dependence on junction capacitance can be seen in Refs. [17] and [43].

The second term P_0 can be obtained by modeling the probe tip as an antenna, and we refer the reader to Ref. [59] for calculation details. The parameters which enter the calculation of P_0 are the principle resonance frequency, ω_0, and damping factor α, in addition to the temperature T. Thus, there are four parameters which determine the $P(E)$-function, T, C_j, ω_0, and α.

The $P(E)$-function can be determined from a fit of the Josephson spectra where the current-voltage characteristics are given by [59,74]

$$I(V) = \frac{\pi e E_J^2}{\hbar}[P(2eV) - P(-2eV)], \tag{13}$$

where E_J is the Josephson energy which can be used as a scaling parameter. Note from Eq. (13) that the zero bias Josephson peak will not represent the overall energy resolution of the tunneling spectrum, because the Josephson peak is given by a *difference* of the $P(E)$-functions which will underestimate the energy resolution. From Eq. (10) the energy resolution is given by a convolution of the $P(E)$ function with the thermal distribution, as discussed below. Figure 31 shows a fit of the $P(E)$-theory to the tunneling spectra in Fig. 26; the Josephson current [Fig. 31(a)] and Josephson dI/dV spectra [Fig. 31(b)], with parameters $T = 15$ mK, $C_j = 11.25$ fF, $\hbar\omega_0 = 17$ μeV, and $\alpha = 2$. We observe that the chosen resonance frequency and damping result in a nice fit of the resonance peak positions of the data, especially seen in Fig. 31(b). The main peak width is also well fit with $T = 15$ mK and $C_j = 11.25$ fF, but we emphasize that these values cannot be used to uniquely determine the temperature as a fit with twice the temperature and twice the capacitance appears to be equally good. This stems from the broadening of the $P(E)$-function which is approximately $\Delta E_{P(E)} \cong 2.35\sqrt{2E_C k_B T}$ [59], whose width is given by the ratio of T/C_j as mentioned above. However, our temperature sensors indicate a temperature of 10-15 mK, and a capacitance value of 11 fF is reasonable for a tunneling probe [75,76]. We discuss a comparison of the $P(E)$ to the thermal broadening, after an application of the $P(E)$-theory to the full tunneling spectrum.

Another application of the $P(E)$-theory is to fit the entire SIS spectrum using Eq. (10), as shown in Fig. 32. Here we show that the coherence peaks appear to be intrinsically limited in width and can no longer be a useful tool for noise estimation once the noise is below their intrinsic broadening. Figure 32 shows three model fits to the data: 1) using the Maki model for the density of states in Eq. (10) [60,61] and without $P(E)$-broadening (green line), 2) using the BCS density of states with $P(E)$ (red line), and 3) using the combined Maki density of states and $P(E)$-

broadening (black line). The details of how good the fits are can be seen in the zoomed in plot of the coherence peak in Fig. 32(b). The Maki model alone (green line) fails to fit the tail of the low energy edge of the coherence peak since there is not a term to give significant broadening (recall temperature does little broadening in SIS junctions). Similarly, using the pure BCS model for the density of states with $P(E)$-broadening fails to fit both tails and overestimates the height of the coherence peak. Finally using a combined model with the Maki density of states and $P(E)$-theory gives the best fit with $T = 15$ mK, the pair breaking parameter $\zeta = 0.012$ and the energy gap $\Delta = 182$ μeV.

Finally, we would like to compare the two broadening functions, $P(E)$ due to the electromagnetic environment and the thermal broadening due to the Fermi distribution, $F(E)$, and their application in future non-SIS tunneling measurements. For non-superconducting tunneling, the $P(E)$ function will become half the width compared to the superconductor case, since $Q = e$ compared to $Q = 2e$, respectively, and Q enters the width of the distribution via the charging energy, as can be seen in Eq. (12). In Fig. 33 we compare these two distributions together with the Fermi thermal broadening distribution, which can be conveniently approximated as

$$F(E) = \frac{1}{(4k_BT)\cosh^2(E/2k_BT)}. \tag{13}$$

From Fig. 33 we observe that the $P(E, Q = e)$ is one half that of $P(E, Q = 2e)$ with $\Gamma_{FWHM} \approx 10.2$ μeV . This is significantly broader than the thermal distribution at 15 mK with $\Gamma_{FWHM} \approx 4.8$ μeV, leading to a resulting convolution (red line in Fig. 32) with $\Gamma_{FWHM} \approx 11.5$ μeV, dominated by the $P(E, Q = e)$ function. In future non-superconducting measurements, we thus expect to reach a resolution that is compatible with this quantum limit and our operating temperature of 10-15 mK, since we know our external noise contribution Γ to the measurement is less than 7-8 μV and this is less than the combined distribution of $P(E, Q = e) * F(E)$, as shown in Fig. 33.

VII. Summary and Conclusions

In this article we have described the design and construction of an instrument which combines STM, AFM, and magnetotransport measurements together in one apparatus operating in a dilution refrigerator at mK temperatures. The instrument allows for simultaneous measurement modalities which span lengths scales and can correlate microscopic variables available via STM and AFM measurements with macroscopic quantum transport measurements. With STM measurements, we demonstrate an instrument resolving capability of less than 8 μeV for tunneling spectroscopy at an operating temperature of 10 mK, which we believe is close to the thermal and quantum operating limits. We have shown in detail how to use SIS Josephson tunneling as a noise detector to examine the various external contributions to the tunneling energy resolution in order to optimize filtering and external electronics.

For force measurements, we showed how to incorporate a qPlus-based AFM in a dilution refrigerator and demonstrate its performance operating at 10 mK and in high magnetic fields. Eddy current damping was shown to lead to a loss in quality factor in high magnetic fields, but this is not detrimental to obtaining high quality and very useful force measurements, particularly in regard to quantum materials such as graphene. Future scientific frontiers will open and flourish as more SPM instruments are developed to operate at ultra-low temperatures and incorporate even further capabilities, such as, electron spin resonance with the STM [77]. We look forward to continued progress and developments with scanning probe microscopy for an ever brighter future.

Acknowledgments

We thank Christian Ast, Alexander Khajetoorians, Vladimir Shvarts, and Nikolai Zhitenev for many useful discussions. We thank Myungchul Oh for his contributions to the cryo-preamp design, and acknowledge Young Jae Song, Jeonghoon Ha, and Hongwoo Baek for initial contributions to the instrumentation. J.S., S.K., D.W., and F.G., acknowledge support under the Cooperative Research Agreement between the University of Maryland and the National Institute of Standards and Technology (NIST), Grant No. 70NANB14H209, through the University of Maryland. M.R.S. acknowledges support under the Cooperative Research Agreement between the Georgetown University and NIST, Grant No. 70NANB18H161, through the NIST/Georgetown PREP program. S.T.L. acknowledges support by NIST and grant 70NANB16H170. S.K. and Y.K acknowledge support in part by the National Research Foundation of Korea Grant (NRF-2010-00349). J.B and F.J.G. acknowledges support by Deutsche Forschungsgemeinschaft, SFB1277, project A02. F.J.G. holds patents on the qPlus sensor. **Data availability**: The data that support the findings of this study are available from the corresponding author upon reasonable request.

DATA AVAILABLITY STATEMENT

The data that support the findings of this study are available from the corresponding author upon reasonable request.

References

[1] I. D. Conway Lamb, J. I. Colless, J. M. Hornibrook, S. J. Pauka, S. J. Waddy, M. K. Frechtling, and D. J. Reilly, Review of Scientific Instruments **87**, 014701 (2016).
[2] B. Patra, R. M. Incandela, J. P. G. van Dijk, H. A. R. Homulle, L. Song, M. Shahmohammadi, R. B. Staszewski, A. Vladimirescu, M. Babaie, F. Sebastiano, and E. Charbon, IEEE Journal of Solid-State Circuits **53**, 309 (2018).
[3] Y. Cao, V. Fatemi, S. Fang, K. Watanabe, T. Taniguchi, E. Kaxiras, and P. Jarillo-Herrero, Nature **556**, 43 (2018).
[4] Y. J. Song, A. F. Otte, Y. Kuk, Y. Hu, D. B. Torrance, P. N. First, W. A. de Heer, H. Min, S. Adam, M. D. Stiles, A. H. MacDonald, and J. A. Stroscio, Nature **467**, 185 (2010).
[5] G. Binnig, C. F. Quate, and Ch. Gerber, Phys. Rev. Lett. **56**, 930 (1986).
[6] N. Moussy, H. Courtois, and B. Pannetier, Rev. Sci. Instrum. **72**, 128 (2001).
[7] H. le Sueur and P. Joyez, Review of Scientific Instruments **77**, 123701 (2006).
[8] H. Kambara, T. Matsui, Y. Niimi, and H. Fukuyama, Rev. Sci. Instrum. **78**, 073703 (2007).
[9] M. Marz, G. Goll, and H. v. Löhneysen, Rev. Sci. Instrum. **81**, 045102 (2010).
[10] Y. J. Song, A. F. Otte, V. Shvarts, Z. Zhao, Y. Kuk, S. R. Blankenship, A. Band, F. M. Hess, and J. A. Stroscio, Review of Scientific Instruments **81**, 121101 (2010).
[11] H. Suderow, I. Guillamon, and S. Vieira, Rev. Sci. Instrum. **82**, 033711 (2011).
[12] S. Misra, B. B. Zhou, I. K. Drozdov, J. Seo, L. Urban, A. Gyenis, S. C. J. Kingsley, H. Jones, and A. Yazdani, Review of Scientific Instruments **84**, 103903 (2013).
[13] M. Assig, M. Etzkorn, A. Enders, W. Stiepany, C. R. Ast, and K. Kern, Review of Scientific Instruments **84**, 033903 (2013).
[14] U. R. Singh, M. Enayat, S. C. White, and P. Wahl, Review of Scientific Instruments **84**, 013708 (2013).
[15] A. Roychowdhury, M. A. Gubrud, R. Dana, J. R. Anderson, C. J. Lobb, F. C. Wellstood, and M. Dreyer, Review of Scientific Instruments **85**, 043706 (2014).
[16] M. Liebmann, J. R. Bindel, M. Pezzotta, S. Becker, F. Muckel, T. Johnsen, C. Saunus, C. R. Ast, and M. Morgenstern, Review of Scientific Instruments **88**, 123707 (2017).
[17] H. von Allwörden, A. Eich, E. J. Knol, J. Hermenau, A. Sonntag, J. W. Gerritsen, D. Wegner, and A. A. Khajetoorians, Review of Scientific Instruments **89**, 033902 (2018).
[18] T. Balashov, M. Meyer, and W. Wulfhekel, Review of Scientific Instruments **89**, 113707 (2018).
[19] T. Machida, Y. Kohsaka, and T. Hanaguri, Review of Scientific Instruments **89**, 093707 (2018).
[20] D. Wong, S. Jeon, K. P. Nuckolls, M. Oh, S. C. J. Kingsley, and A. Yazdani, Review of Scientific Instruments **91**, 023703 (2020).
[21] H. Baek, J. Ha, D. Zhang, B. Natarajan, J. P. Winterstein, R. Sharma, R. Hu, K. Wang, S. Ziemak, J. Paglione, Y. Kuk, N. B. Zhitenev, and J. A. Stroscio, Phys. Rev. B **92**, 094510 (2015).
[22] M. Hashisaka, Y. Yamauchi, K. Chida, S. Nakamura, K. Kobayashi, and T. Ono, Review of Scientific Instruments **80**, 096105 (2009).
[23] A. Lukashenko and A. V. Ustinov, Review of Scientific Instruments **79**, 014701 (2008).
[24] D. V. Pelekhov, J. B. Becker, and Jr. Nunes, Rev. Sci. Instrum. **70**, 114 (1999).
[25] K. R. Brown, L. Sun, and B. E. Kane, Rev. Sci. Instrum. **75**, 2029 (2004).

[26] A. E. Gildemeister, T. Ihn, C. Barengo, P. Studerus, and K. Ensslin, Rev. Sci. Instrum. **78**, 013704 (2007).
[27] B. Hackens, F. Martins, S. Faniel, C. A. Dutu, H. Sellier, S. Huant, M. Pala, L. Desplanque, X. Wallart, and V. Bayot, Nature Communications **1**, 39 (2010).
[28] R. J. Celotta, S. B. Balakirsky, A. P. Fein, F. M. Hess, G. M. Rutter, and J. A. Stroscio, Review of Scientific Instruments **85**, 121301 (2014).
[29] Chr. Wittneven, R. Dombrowski, S. H. Pan, and R. Wiesendanger, Rev. Sci. Instrum. **68**, 3806 (1997).
[30] S. H. Pan, WO/1993/019494.
[31] EBL #4, Staveley Sensors, Inc., EBL Product Line, E. Hartford, CT.
[32] Model WMG40-340-95-EMS, Ferrovac GmbH, CH 8050 Zurich, Switzerland.
[33] Tungsten alloy HD17, Mi-Tech Metals, 4701 Massachusetts Ave., Indianapolis, Indiana 46218, USA., (n.d.).
[34] Model RECOM and SHOMFerrovac GmbH, CH 8050 Zurich, Switzerland.
[35] S. B. Field and J. Barentine, Review of Scientific Instruments **71**, 2603 (2000).
[36] Model JDR-500, Janis Research Company, Inc., Wilmington, MA.
[37] New England Wire, Lisbon, NH.
[38] Johnson/Cinch SMP connector 127-1711-601, Mouser part number 530-127-1711-601 1000, North Main Street, Mansfield, TX 76063, USA.
[39] J. M. Martinis, M. H. Devoret, and J. Clarke, Phys. Rev. B **35**, 4682 (1987).
[40] A. Fukushima, A. Sato, A. Iwasa, Y. Nakamura, T. Komatsuzaki, and Y. Sakamoto, IEEE Transactions on Instrumentation and Measurement **46**, 289 (1997).
[41] K. Bladh, D. Gunnarsson, E. Hürfeld, S. Devi, C. Kristoffersson, B. Smålander, S. Pehrson, T. Claeson, P. Delsing, and M. Taslakov, Review of Scientific Instruments **74**, 1323 (2003).
[42] F. P. Milliken, J. R. Rozen, G. A. Keefe, and R. H. Koch, Review of Scientific Instruments **78**, 024701 (2007).
[43] Discoidal Capacitors 150 OD, NPO, 2000pf, K, 500 V, Part number 150045EN202K6B0, API Technologies Company Headquarters, 400 Nickerson Road, Marlborough, MA 01752, USA.
[44] Part number CU226020, Goodfellow Corporation, 125 Hookstown Grade Road, Coraopolis, PA 15108-9302, USA.
[45] J.-F. Ge, M. Ovadia, and J. E. Hoffman, Review of Scientific Instruments **90**, 101401 (2019).
[46] F. J. Giessibl, Appl. Phys. Lett. **73**, 3956 (1998).
[47] F. Huber and F. J. Giessibl, Review of Scientific Instruments **88**, 073702 (2017).
[48] Model AD 8616, Analog Devices, Technology Way, P.O. Box 9106, Norwood, MA 02062-9106, USA.
[49] F. J. Giessibl, Review of Scientific Instruments **90**, 011101 (2019).
[50] T. R. Albrecht, P. Grütter, D. Horne, and D. Rugar, Journal of Applied Physics **69**, 668 (1991).
[51] K. Kobayashi, H. Yamada, and K. Matsushige, Review of Scientific Instruments **80**, 043708 (2009).
[52] F. J. Giessibl, Appl. Phys. Lett. **78**, 123 (2000).
[53] G. H. Simon, M. Heyde, and H.-P. Rust, Nanotechnology **18**, 255503 (2007).
[54] F. J. Giessibl, Rev. Mod. Phys. **75**, 949 (2003).
[55] M. Človečko and P. Skyba, Appl. Phys. Lett. **115**, 193507 (2019).

[56] S. Jung, G. M. Rutter, N. N. Klimov, D. B. Newell, I. Calizo, A. R. Hight-Walker, N. B. Zhitenev, and J. A. Stroscio, Nat Phys **7**, 245 (2011).
[57] D. Walkup, F. Ghahari, C. Gutiérrez, K. Watanabe, T. Taniguchi, N. B. Zhitenev, and J. A. Stroscio, Phys. Rev. B **101**, 035428 (2020).
[58] S. Kim et al. (to be published).
[59] C. R. Ast, B. Jäck, J. Senkpiel, M. Eltschka, M. Etzkorn, J. Ankerhold, and K. Kern, Nat Commun **7**, 1 (2016).
[60] K. Maki and T. Tsuneto, Progress of Theoretical Physics **31**, 945 (1964).
[61] D. C. Worledge and T. H. Geballe, Phys. Rev. B **62**, 447 (2000).
[62] H. Huang, C. Padurariu, J. Senkpiel, R. Drost, A. L. Yeyati, J. C. Cuevas, B. Kubala, J. Ankerhold, K. Kern, and C. R. Ast, ArXiv:1912.08901 [Cond-Mat] (2019).
[63] Model SA-606F2, NF Corporation, 6-3-20 Tsunashima Higashi, Kohoku-ku, Yokohama 223-8508, Japan.
[64] Model DLPCS-100, Femto Messtechnik GmbH, Klosterstraße 64, 10179 Berlin, Germany., (n.d.).
[65] Model 1211, DL Instruments, Ithaca, NY, USA.
[66] Nanonis SPM control system, SPECS Zurich GmbH, Technoparkstrasse 1, 8005 Zurich, Switzerland.
[67] Model AD 524, Analog Devices, Technology Way, P.O. Box 9106, Norwood, MA 02062-9106, USA.
[68] Model AD OP77E, Analog Devices, Technology Way, P.O. Box 9106, Norwood, MA 02062-9106, USA.
[69] Model SLP-1.9+, Mini-Circuits, P.O. Box 350166, Brooklyn, NY 11235-0003, USA.
[70] Model 3076, KR Electronics, 91 Avenel Street, Avenel, NJ 07001, USA.
[71] Model CN060412, Toroid Corporation, 2020 Northwood Drive, Salisbury, MD 21801, USA.
[72] Model 56-705-002, API TECHNOLOGIES, 8061 Avonia Rd., Fairview, PA 16415, USA.
[73] Model 370, Lake Shore Cryotronics, 575 McCorkle Blvd., Westerville, OH 43082-8699, USA.
[74] D. V. Averin, Yu. V. Nazarov, and A. A. Odintsov, Physica B: Condensed Matter **165–166**, 945 (1990).
[75] S. Kurokawa and A. Sakai, Journal of Applied Physics **83**, 7416 (1998).
[76] J. M. de Voogd, M. A. van Spronsen, F. E. Kalff, B. Bryant, O. Ostojić, A. M. J. den Haan, I. M. N. Groot, T. H. Oosterkamp, A. F. Otte, and M. J. Rost, Ultramicroscopy **181**, 61 (2017).
[77] W. Paul, S. Baumann, C. P. Lutz, and A. J. Heinrich, Review of Scientific Instruments **87**, 074703 (2016).
[78] The error represents one standard deviation in the measured quantity.

Tables:

TABLE 1: Comparison of AFM performance metrics between UHV systems operating at 4 K [47] and the mK instrument described in this article. Common parameters for all cases are $A = 50\ \mathrm{pm}$, $f_0 = 30\ \mathrm{kHz}$, and $k = 1800\ \mathrm{N/m}$. For both the LT and ULT systems the detector

noise, $\delta k_{ts\,det}$, dominates the total AFM noise. Although the deflection noise is larger for the ULT case due to the larger AFM preamp noise level, it can be compensated by operating at a lower bandwidth to achieve a comparable noise level (see third column).

Parameter	UHV LT($B_W = 10$ Hz)	UHV ULT ($B_W = 10$ Hz)	UHV ULT ($B_W = 2.5$ Hz)
T (K)	4.2	0.01	0.01
Q	200 000	200 000	200 000
n_{el} $(\mu V/\sqrt{Hz})$	0.136	1.44	1.44
n_q $(fm/\sqrt{Hz})$	24	168	168
$\delta k_{ts\,det}(mN/m)$	1.5	10.4	1.3
$\delta k_{ts\,th}(mN/m)$	0.3	0.018	0.018
$\delta k_{ts\,osc}(mN/m)$	.02	0.135	0.0678
$\delta k_{ts\,sum}(mN/m)$	1.5	10.4	1.3

Figure Captions:

Figure 1: Computer-aided design (CAD) model of the SPM module in an exploded view showing the various internal components. The main housing and top compression stage of the SPM module is constructed from molybdenum, except for the bottom electrical plug which is fabricated from gold-plated coin silver.

Figure 2: Photo of the SPM inside the room temperature UHV chamber above the DR showing the components outlined in Fig. 1.

Figure 3: CAD model of (a) the sample and tip receptacle, (b) sample holder inside the receptacle, and (c) tip holder inside the receptacle. The parts colored green in the receptacle are made from molybdenum, as well as the dark blue sample and tip holder parts. The pink parts on top of the receptacle are made from alumina. The light blue Allen screw housing is made from silicon bronze. The beryllium-copper clamp spring is activated upwards/downwards (red arrow) by turning the Allen screw using a wobble stick fitted with an Allen driver [32].

Figure 4: Photographs of (a) sample holder inside of the sample receptacle and (b) a transfer receptacle to move samples and probes through the various UHV systems. 1 MΩ surface mount resistors are seen on top of the transfer receptacle near the end of each beryllium-copper finger spring to ground each lead and avoid static charge buildup during transfers.

Figure 5: CAD model showing the *X*-*Y* capacitive position sensor and tip stage inside the SPM module (note this view is upside down). The large moving electrode of the position sensor is attached to a piece of the tip stage shown in Fig. 3(c).

Figure 6: Photograph of the dilution refrigerator [36]. New additions to the previous instrument [10] include the cryogenic STM and AFM preamps attached to the IVC flange, press-style heat sinks, RF powder filters, and a mechanical thermal switch, facilitating the cooling process after loading the microscope module to the tail section.

Figure 7: Photographs of RF powder filters in various stages of construction. (a) 4 mil polyimide coated copper wire is shown wound around epoxy-metal powder core and one end attached to the SMP connector [38]. (b) Final central core of a plain filter is assembled with both ends attached to SMP connectors. (c) Parts shown before potting consisting of central core, main housing, and top cap. On the right is shown a final assembled powder filter. (d) The π-version of the powder filter is shown in mid-construction phase. The key difference is the discoidal capacitor (silver disk) [43] attached to the bottom of SMP connector. (e) Powder filters attached to an adaptor plate on the mixing chamber showing cables attached to them via SMP connectors.

Figure 8: Transmission vs. frequency measurements of the two types of RF powder filters measured at room temperature.

Figure 9: Schematic of the preamp electronics at the various thermal stages at 10 mK, 4 K, and 300 K. The solid red and blue lines denote shielded twisted pair cables. The selection of internal vs. external preamps is made by wiring the probe tip to different contacts on the tip holder. When the internal preamp is selected the tunneling bias is applied to the tip with the sample grounded, whereas when the external preamp is selected the bias is applied to the sample with the tip at virtual ground.

Figure 10: Photograph of the floating cryogenic preamp consisting of the ceramic circuit board inside a box driven at reference potential (tunnel bias), which is then contained inside another box at cryostat ground. The preamp can be seen mounted to the IVC flange in Fig. 6.

Figure 11: AFM preamplifier spectral noise density vs. frequency. Probe tip retracted, not in feedback. AFM settings: oscillation amplitude 200 pm, 10 Hz PLL B_W, 48.6 Hz cutoff. T = 10 mK.

Figure 12: STM preamplifier spectral noise density vs. frequency. Probe tip retracted, not in feedback. T = 10 mK.

Figure 13: Schematic of qPlus sensor designed for mK AFM and STM measurements. Sensor parameters (see qPlus sensor S1.0B in Ref. [49]), length 2360 µm, height 214 µm, width 127 µm, force constant $\mathrm{k} = 1800$ Nm, resonance frequency, $\mathrm{f}_0 = 33$ kHz, charge per deflection 2.8 aC/pm, charge per force 1.5 aC/nN. Measured sensitivity $\mathrm{S_V} = (8.66 \pm 0.01)\ \mu\mathrm{V/pm}$ [78].

Figure 14: (a) CAD model of tip stage with tuning fork sensor. The tuning fork sensor (green) is epoxied to a quartz plate (red) with predefined electrode pattern for the AFM and STM signals. A second quartz plate is used for the excitation signal. Both quartz plates are epoxied to a molybdenum “T” insert which is screwed into the tip holder plate via 1 mm screws (not shown). (b) Photograph of qPlus sensor and sample in the SPM module in the upper UHV chamber.

Figure 15: Sensor Q-value response changes with tightening the tip holder inside the tip receptacle using the Allen screw activation of the beryllium-copper spring plate [see Fig. 3(a)]. Measurements made at T = 300 K in the upper UHV chamber before loading the SPM module into the DR. This is a standard procedure which is followed.

Figure 16: (black symbols) Measured Z servo response in feedback vs AFM oscillator amplitude drive signal. (red line) Linear fit to the data for values above 40 mV amplitude which yields a slope value of (115.5 ± 0.1) nm V^{-1} [78]. AFM feedback frequency shift setpoint –3 Hz.

Figure 17: (black symbols) Frequency shift spectral noise density vs frequency. (red line) Linear fit to the data for values between 4 Hz and 200 Hz which yields a slope value of $(2.48 \pm 0.02) \times 10^{-3}$ Hz$^{-1/2}$ [78]. AFM settings: oscillation amplitude 97 pm, 1 kHz PLL B_W, 6.23 kHz cutoff.

Figure 18: Noise spectral density vs. sensor quality factor Q from the three main noise sources in the AFM measurement comprising the detector noise $\delta\mathrm{k_{ts\,det}}$, the oscillator noise $\delta\mathrm{k_{ts\,osc}}$, and the thermal noise $\delta\mathrm{k_{ts\,th}}$, and their sum $\delta\mathrm{k_{ts\,sum}}$. The noise is shown for two bandwidths (dashed line) B_W = 10 Hz, and (solid line) B_W = 2.5 Hz. The thermal noise is calculated for a temperature of $\mathrm{T} = 15$ mK.

Figure 19: AFM qPlus sensor response in high magnetic fields. (a) Amplitude vs. frequency for field values ranging from 0 T to 7 T, (b) (symbols) shift in amplitude peak center frequency vs. magnetic field, (line) linear fit with a slope value of (0.025 ± 0.002) Hz T^{-1} [78], (c) Q factor vs. magnetic field B, and (d) (symbols) $1/Q$ vs B^2 showing a linear relationship with a linear fit (line) with a slope value of $(9.52 \pm 0.09) \times 10^{-7}$ T^{-2} [78].

Figure 20: Simultaneous AFM and STM imaging at 10 mK. (a) AFM topographic signal. AFM setpoints: oscillation amplitude 300 pm, frequency setpoint -3.5 Hz, sample bias -18 mV. (b) STM current signal obtained simultaneously with (a). (c) Atomic resolution AFM image of the Al(111) surface. AFM parameters: oscillation amplitude 500 pm, frequency shift setpoint -33 Hz, sample bias 10 mV.

Figure 21: Graphene heterostructure device in Hall bar geometry. (a) Photograph of the device. Various hBN crystal layers are seen in turquoise color along with six electrodes including the landing pad guiding runway. (b) A zoomed in portion of the Hall bar device showing the contacts along with a schematic of the reactive ion-etched graphene layer (grey). Four 1 μm × 1 μm AFM images are shown near the graphene/hBN boundaries, the top two (i) and (ii) are constant height AFM images, oscillation amplitude 2 nm, sample bias 300 mV, gate voltage -40 V, and the bottom two (iii) and (iv) are constant frequency shift images, oscillation amplitude 2 nm, frequency shift setpoint -40 mHz, sample bias 100 mV. The scan speeds were (i) 250 nm/s, (ii) 180 nm/s, and 60 nm/s for both (iii) and (iv). In both cases a strong contrast is obtained between the graphene and hBN regions which can be used to obtain STM images right up to the conducting edges to measure edge state electronic structure. (c) Scan of the graphene surface in STM feedback. STM settings for large scan, $I_{set} = 10$ pA, $V_B = 300$ mV, for small scan in inset, $I_{set} = 20$ pA, $V_B = 500$ mV.

Figure 22: Hall resistance vs. back gate voltage and magnetic field measured across terminals 1 and 4 when applying the current between terminals 5 and 6 in Fig. 21. The conductance shows the expected plateaus at the various filling factors, ν, for the graphene quantum Hall effect.

Figure 23: Scanning tunneling spectroscopy *dI*/*dV* map vs. sample bias and back gate voltage at $B = 4$ T obtained on the graphene Hall bar in Fig. 21. For a fixed gate voltage, Landau levels are seen as a series of peaks in the *dI*/*dV* measurements. Diamonds appear the Fermi level (zero bias) at gate values corresponding to integer filling factor due to the bulk of the sample going into a Hall insulator, thereby creating a voltage divider between the vacuum tunnel junction and the graphene sample. STM settings: $I_{set} = 200$ pA, $V_B = 300$ mV, $V_{mod} = 360$ μV, $f_{mod} = 334$ Hz. $T = 10$ mK.

Figure 24: (symbols) *dI*/*dV* tunneling spectra of an aluminum sample and 0.25 mm diameter iridium probe tip at a sample temperature of $T = 10$ mK prior to the improvements described in this paper. Tunneling conditions: current setpoint $I_{set} = 200$ pA, sample bias $V_B = 1$ mV, modulation voltage, $V_{mod} = 10$ μV, modulation frequency, $f_{mod} = 141$ Hz. (line) Best fit to the Maki equations with an effective temperature of $T_{eff} = 230$ mK, an energy gap of $\Delta = (180.6 \pm 0.6)$ μeV, and a depairing parameter of $\zeta = (0.029 \pm 0.001)$. The effective temperature in the fit corresponds to a voltage noise broadening of $\approx 3.5k_BT \approx 70$ μeV. The aluminum sample was grown *in-situ* using molecular beam epitaxy from a source onto a graphene/SiC substrate. The aluminum film thickness was nominally 100 nm.

Figure 25: dI/dV tunneling spectra of an aluminum sample and a 0.8 mm diameter aluminum probe tip at a sample temperature of T ≈ 10 mK. Tunneling conditions: $I_{set} = 5$ nA, $V_B = 2$ mV, $V_{mod} = 1.5$ μV, $f_{mod} = 112$ Hz.

Figure 26: Josephson tunneling of an aluminum sample and tip in the low bias tunneling range. (a) Current vs. sample bias showing a valley-to-peak transition width of ≈ 11 μV along with oscillations between $\pm$(15-20)μV. (b) dI/dV vs. sample bias showing $\Gamma_{Zero} \approx 10.6$ μV, $\Gamma_{FWHM} \approx 7.6$ μV of the zero bias Josephson peak. Tunneling conditions: $I_{set} = 5$ nA, $V_B = 2$ mV, $V_{mod} = 1.5$ μV, $f_{mod} = 112$ Hz.

Figure 27: dI/dV tunneling spectra of an aluminum sample and tip as a function of tunneling impedance. (a) Large voltage range spectra. (b) Zoomed in range covering the left coherence peak. The coherence peak is observed to decrease in peak height and broadened with a decrease in tunnel junction impedance. Tunneling conditions: $V_B = 1.5$ mV, $V_{mod} = 1.5$ μV, $f_{mod} = 112$ Hz. Tunneling currents for impedances 300 kΩ to 10 MΩ: 5 nA, 1.5 nA, 0.5 nA, and 0.15 nA.

Figure 28: dI/dV tunneling spectra of an aluminum sample and tip as a function of external transimpedance preamplifier. (a) Large voltage range spectra. Tunneling conditions: $I_{set} = 500$ pA, $V_B = 1.5$ mV, $V_{mod} = 1.5$ μV, $f_{mod} = 112$ Hz. (c) Zoomed in range from (a) covering the coherence peak at negative sample bias. (c) Zoomed in range covering the zero bias Josephson peak. Tunneling conditions: $I_{set} = 5$ nA, $V_B = 1.5$ mV, $V_{mod} = 1.5$ μV, $f_{mod} = 112$ Hz. The various preamplifiers contribute different amounts of noise to the tunneling junction. Preamplifier "A" NF SA-606F2 [60] yields $\Gamma_{Zero} \approx 10.6$ μV, $\Gamma_{FWHM} \approx 7.9$ μV, "B" FEMTO DLPCS-100 [61] $\Gamma_{Zero} \approx 43$ μV, $\Gamma_{FWHM} \approx 25$ μV and "C" DL 1211 [65] $\Gamma_{Zero} \approx 53$ μV, $\Gamma_{FWHM} \approx 36$ μV.

Figure 29: dI/dV tunneling spectra of an aluminum sample and tip as a function of external RF filters on the sample bias input line. Tunneling conditions: $I_{set} = 5$ nA, $V_B = 2$ mV, $V_{mod} = 1.5$ μV, $f_{mod} = 112$ Hz. The different filters reject different amounts of noise which can be measured by the zero crossing and FWHM of the Josephson peak. Filter A: $\Gamma_{Zero} \approx 10.6$ μV, $\Gamma_{FWHM} \approx 7.8$ μV, Filter B: $\Gamma_{Zero} \approx 13$ μV, $\Gamma_{FWHM} \approx 8.8$ μV, Filter C: $\Gamma_{Zero} \approx 14$ μV, $\Gamma_{FWHM} \approx 9.3$ μV, Filter D: $\Gamma_{Zero} \approx 45$ μV, $\Gamma_{FWHM} \approx 28$ μV, Filter E: $\Gamma_{Zero} \approx 53$ μV, $\Gamma_{FWHM} \approx 36$ μV.

Figure 30: dI/dV tunneling spectra of an aluminum sample and tip of the right coherence peak with the piezo-motor port on the UHV (brown) connected to the piezo-motor controller and (red) grounded to the cryostat. Tunneling conditions: $I_{set} = 500$ pA, $V_B = 2$ mV, $V_{mod} = 12$ μV, $f_{mod} = 112$ Hz.

Figure 31: Josephson tunneling measurements (symbols) of an aluminum sample and tip in the low bias tunneling range with fits to P(E)-theory (line) for the measurements of (a) current vs sample bias, and (b) dI/dV vs sample bias. Tunneling setpoints: $I_{set} = 5$ nA, $V_B = 2$ mV, $V_{mod} = 1.5$ μV, $f_{mod} = 112$ Hz.

Figure 32: *dI*/*dV* tunneling spectra of an aluminum sample and tip with fits to various models. (a) Large bias range spectra; tunneling conditions: $I_{set} = 150$ pA, $V_B = 1.5$ mV, $V_{mod} = 1.5$ μV, $f_{mod} = 112$ Hz. (b) Zoomed in region of left coherence peak. Parameters used for the calculations are: Maki model, $T = 15$ mK, $\zeta = 0.017$, $\Delta = 185$ μeV; $P(E)$ model, $T = 15$ mK, $C_j = 11.25$ fF, $\omega_0 = 17$ μeV; combined Maki-$P(E)$ model, $T = 15$ mK, $\zeta = 0.012$, $\Delta = 182$ μeV, $C_j = 11.25$ fF, $\omega_0 = 17$ μeV. See main text for discussion.

Figure 33: A comparison of probability distributions for $P(E)$ and temperature. The $P(E)$ distribution for single charge $Q = e$ is half the width than for Cooper pairs, $Q = 2e$. The convolution of $P(E)$ and the temperature distribution will give the ultimate energy resolution for tunneling, which is shown to be ≈ 11.5 μeV at $T = 15$ mK, which is within our ability to resolve with the current noise level of the instrument, which is below 8 μV. Parameters for $P(E)$ model, $T = 15$ mK, $C_j = 11.25$ fF, $\omega_0 = 17$ μeV.

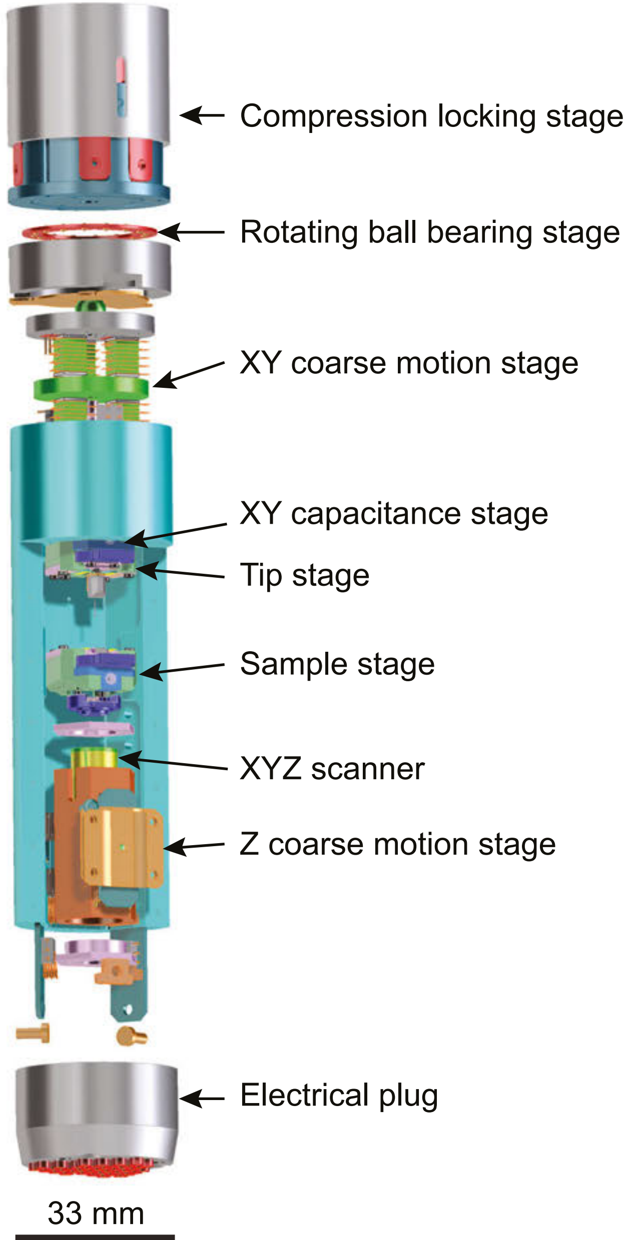
Compression locking stage
Rotating ball bearing stage
XY coarse motion stage
XY capacitance stage
Tip stage
Sample stage
XYZ scanner
Z coarse motion stage
Electrical plug
33 mm

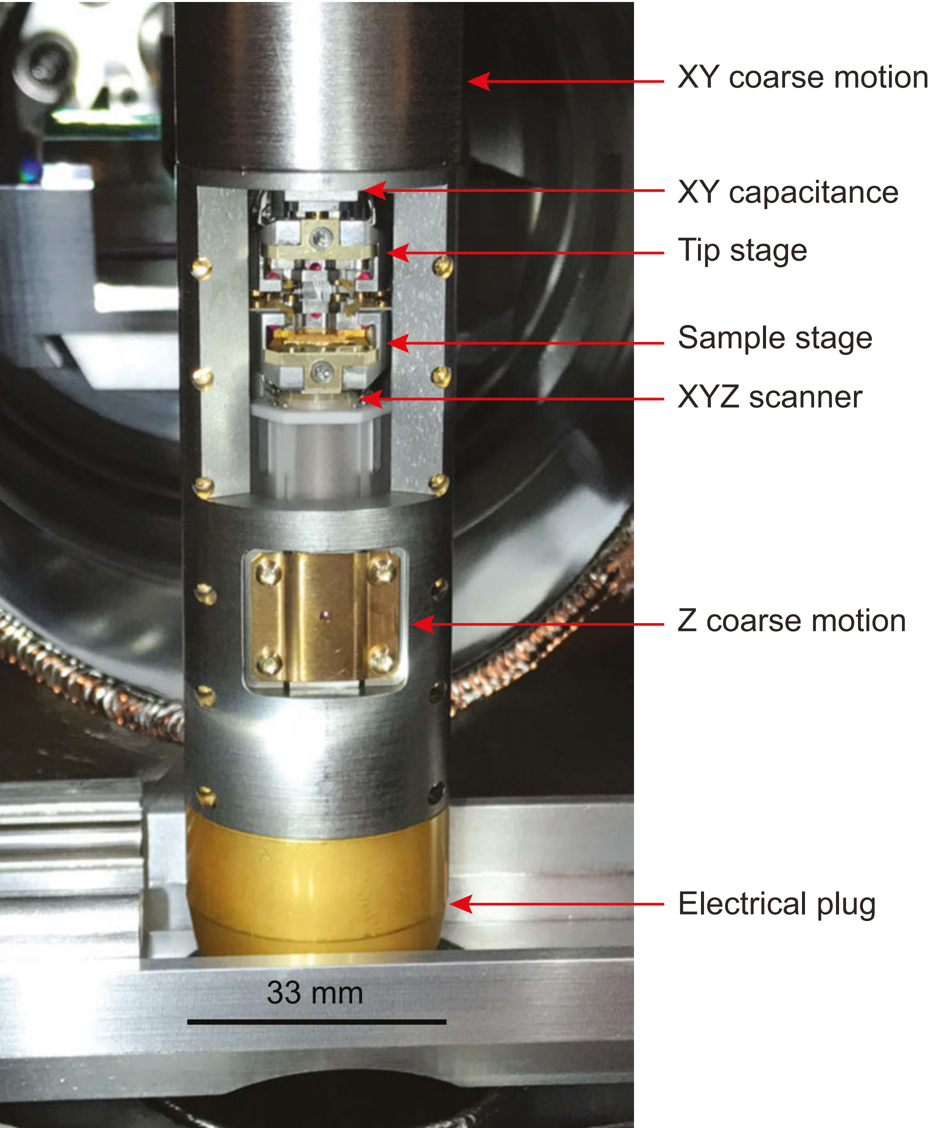
XY coarse motion
XY capacitance
Tip stage
Sample stage
XYZ scanner
Z coarse motion
Electrical plug
33 mm

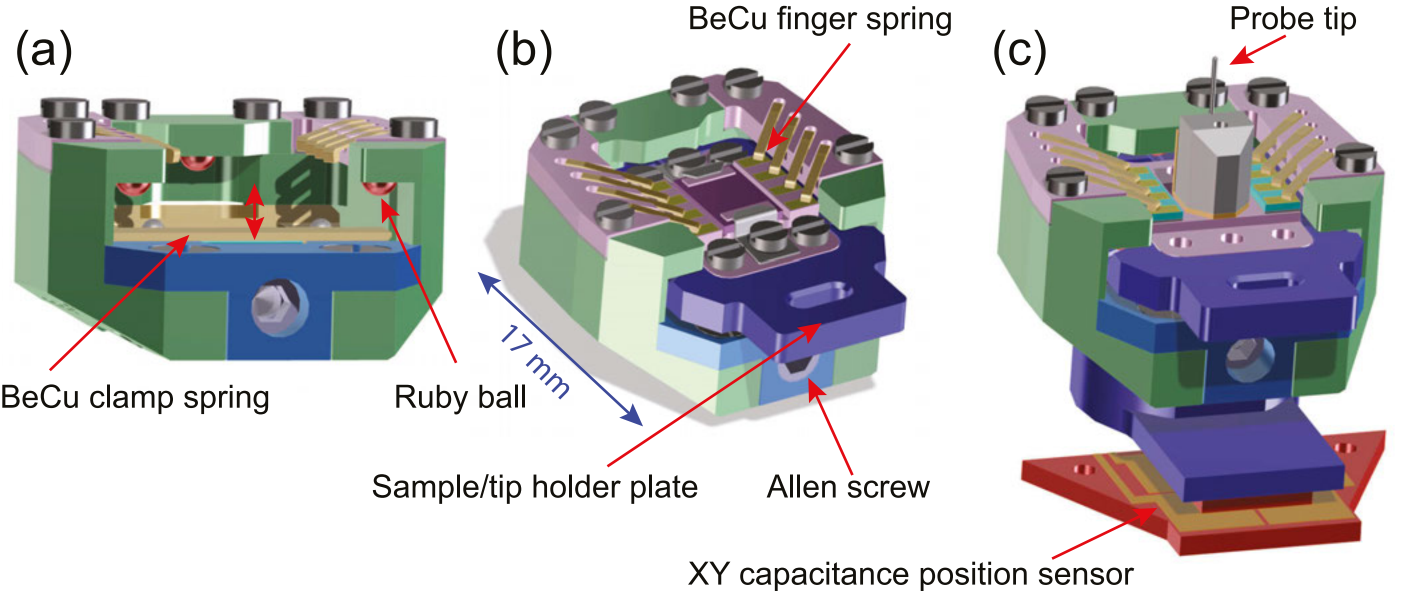
(a)
(b)
(c)
BeCu finger spring
Probe tip
BeCu clamp spring
Ruby ball
17 mm
Sample/tip holder plate
Allen screw
XY capacitance position sensor

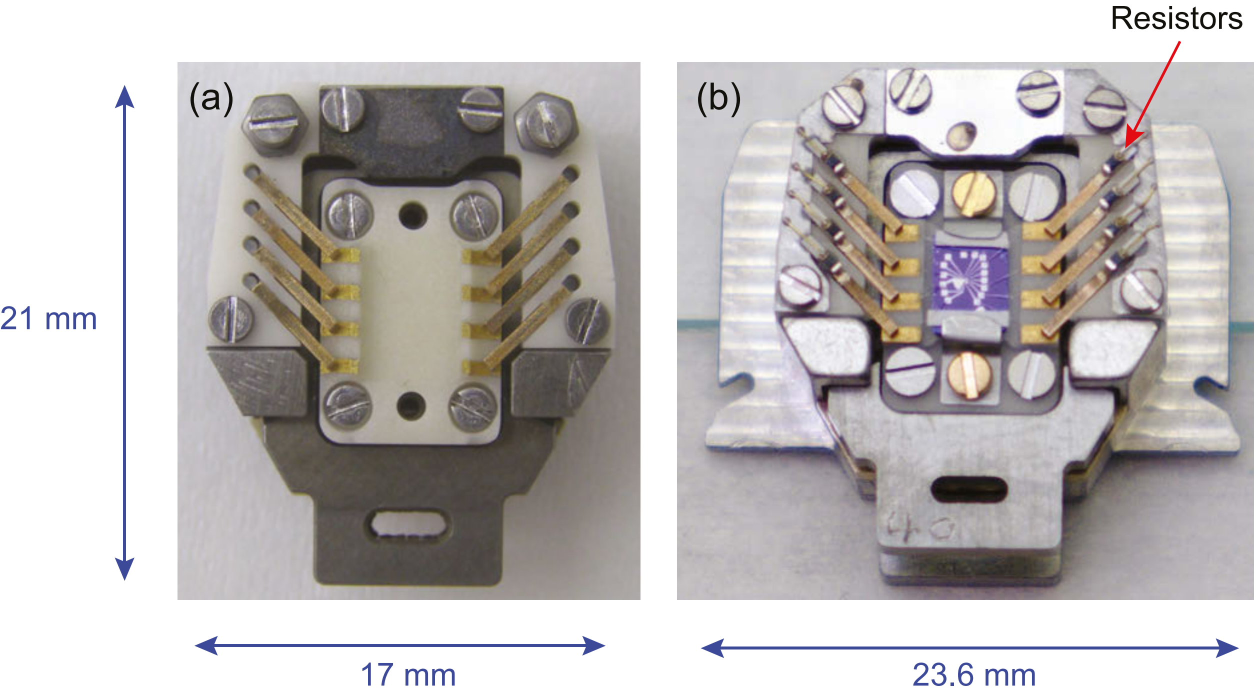

Resistors
(a)
(b)
21 mm
17 mm
23.6 mm

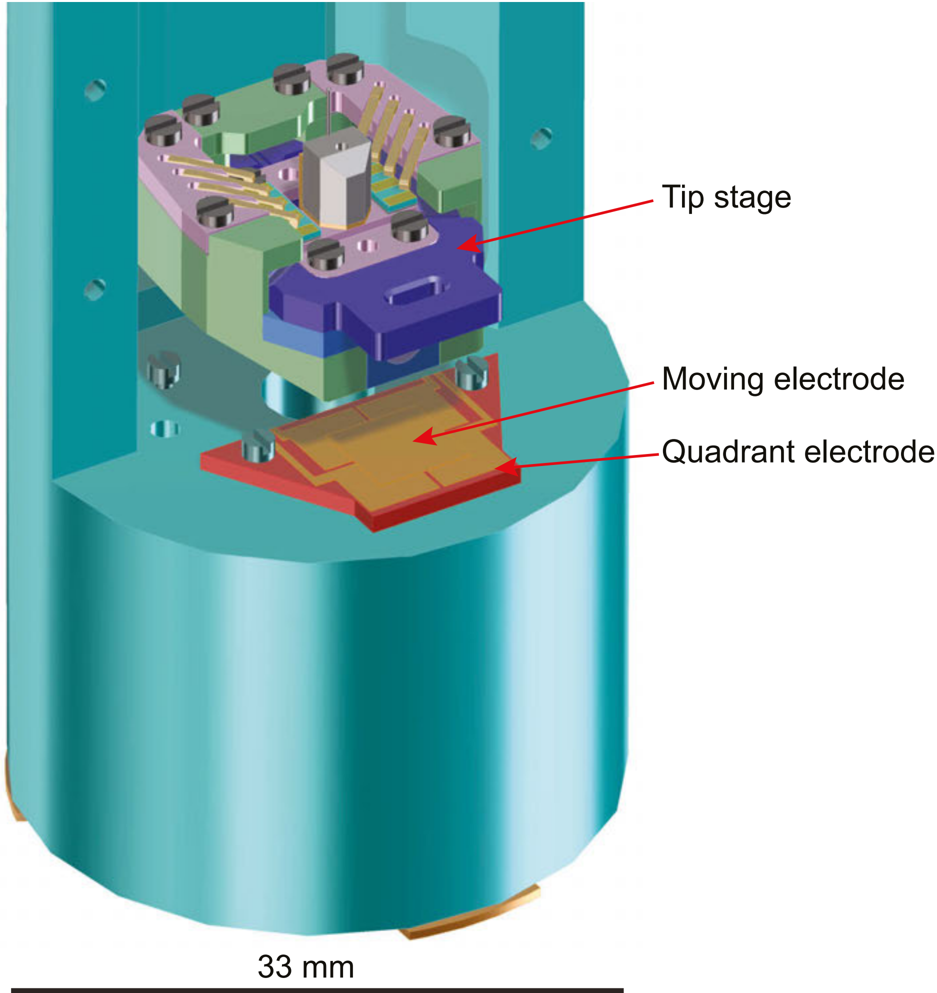
Tip stage
Moving electrode
Quadrant electrode
33 mm

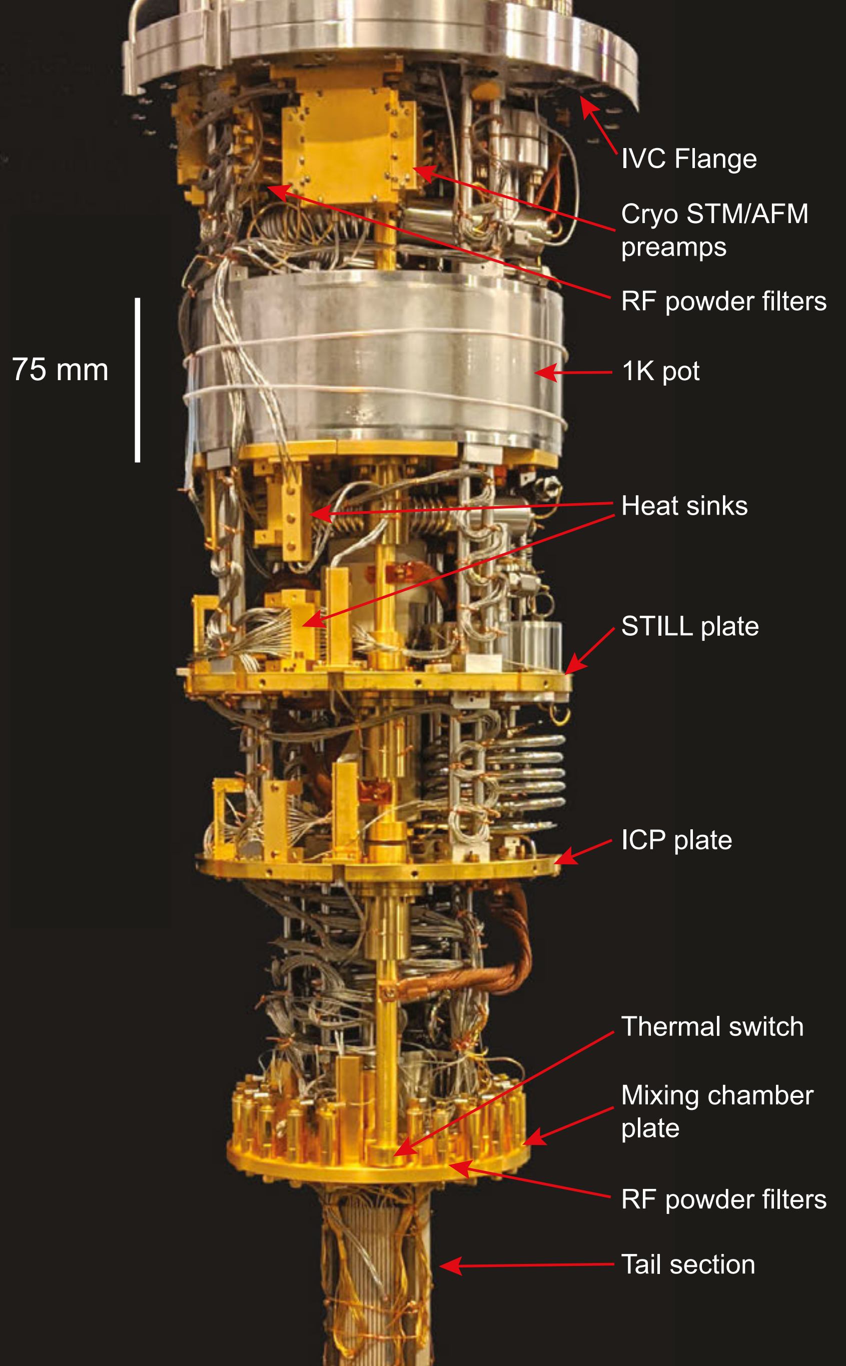

IVC Flange
Cryo STM/AFM preamps
RF powder filters
75 mm
1K pot
Heat sinks
STILL plate
ICP plate
Thermal switch
Mixing chamber plate
RF powder filters
Tail section

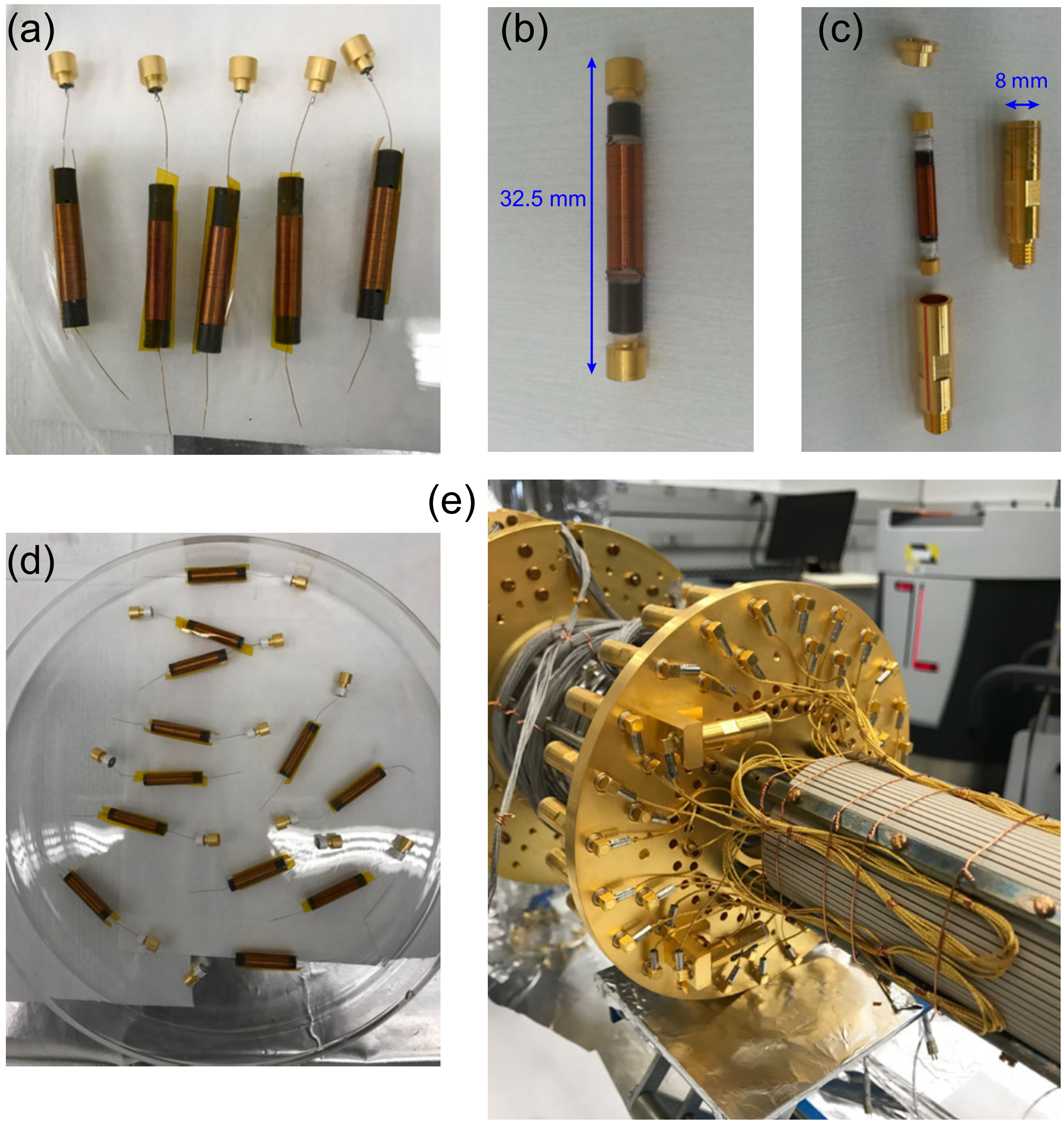
(a)
(b)
32.5 mm
(c)
8 mm
(d)
(e)

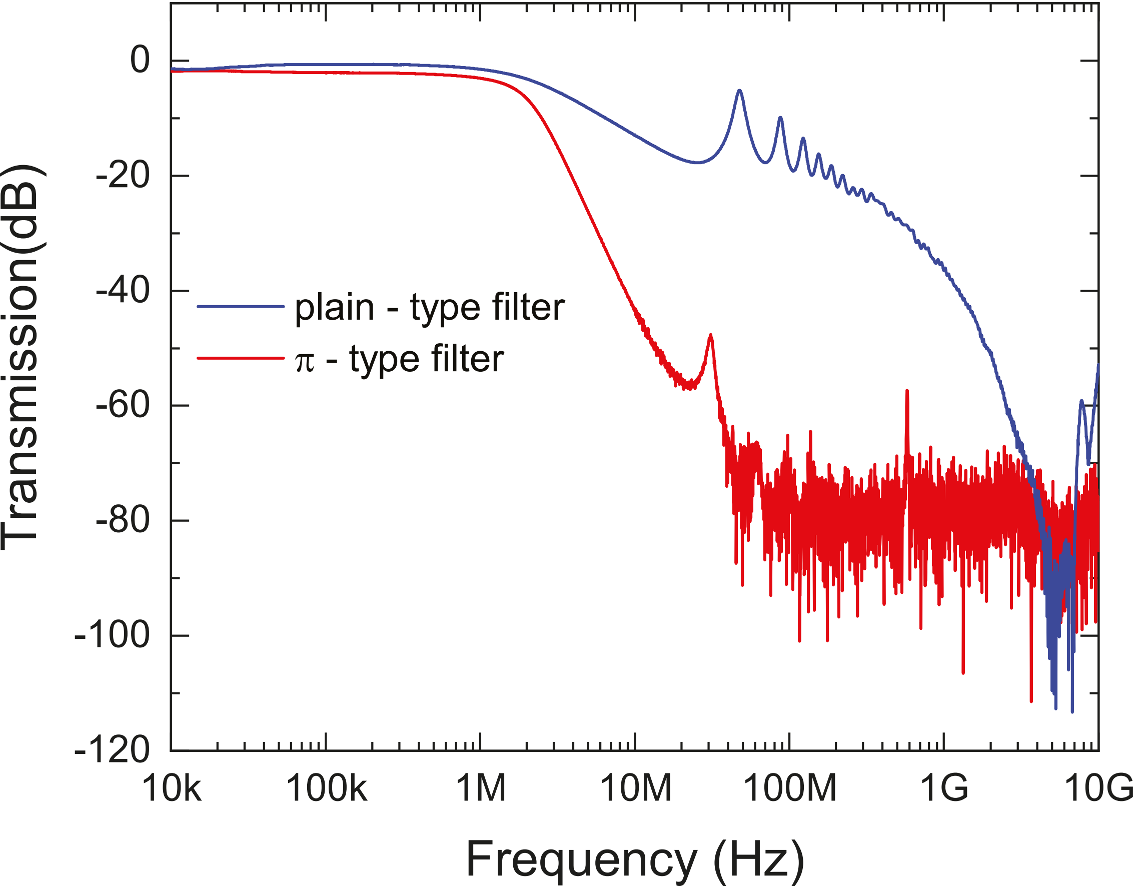

Transmission(dB)
0
-20
-40
-60
-80
-100
-120
10k
100k
1M
10M
100M
1G
10G
Frequency (Hz)
plain - type filter
π - type filter

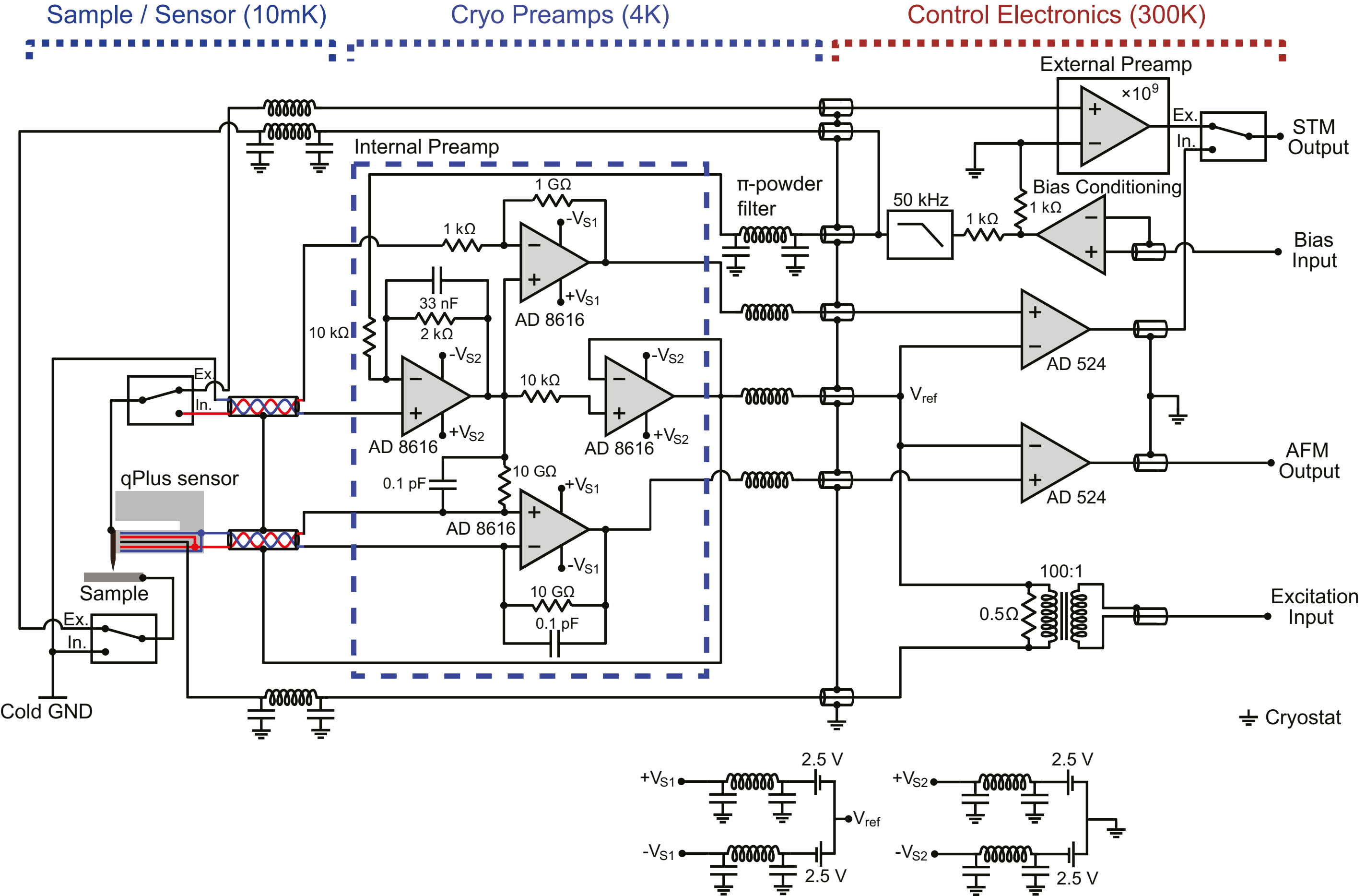

Sample / Sensor (10mK)
Cryo Preamps (4K)
Control Electronics (300K)
External Preamp
×10^9
Ex.
In.
STM Output
Internal Preamp
π-powder filter
50 kHz
1 kΩ
Bias Conditioning
1 kΩ
Bias Input
1 GΩ
1 kΩ
-VS1
+VS1
AD 8616
33 nF
2 kΩ
10 kΩ
-VS2
+VS2
AD 8616
10 kΩ
-VS2
+VS2
AD 8616
AD 524
Vref
AD 524
AFM Output
Ex
In.
qPlus sensor
0.1 pF
10 GΩ
+VS1
AD 8616
-VS1
10 GΩ
0.1 pF
Sample
Ex.
In.
100:1
0.5Ω
Excitation Input
Cold GND
Cryostat
+VS1
2.5 V
Vref
-VS1
2.5 V
+VS2
2.5 V
-VS2
2.5 V

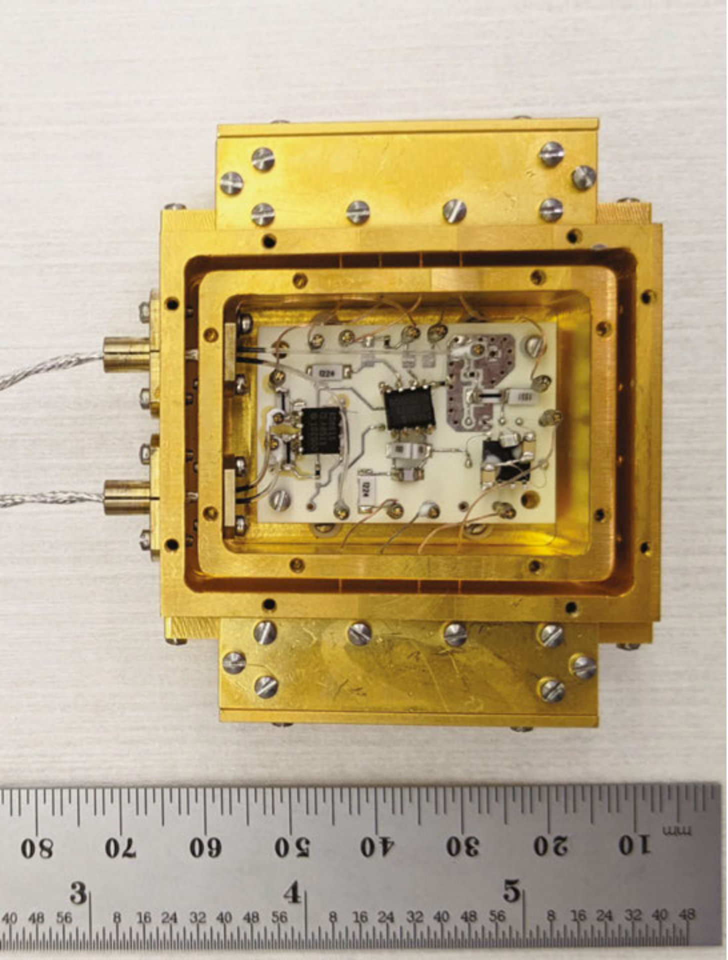
3
4
5

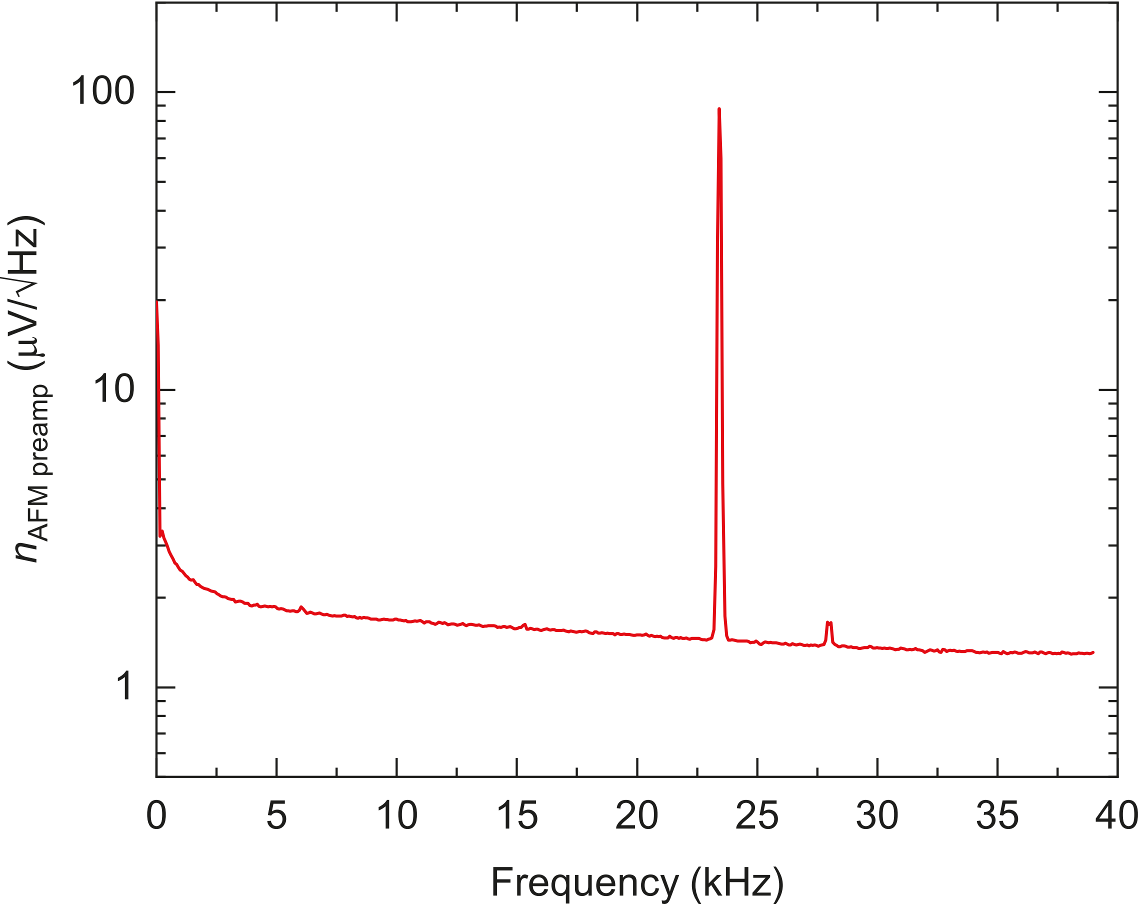
100
10
1
$n_{\mathrm{AFM\ preamp}}$ (μV/√Hz)
0
5
10
15
20
25
30
35
40
Frequency (kHz)

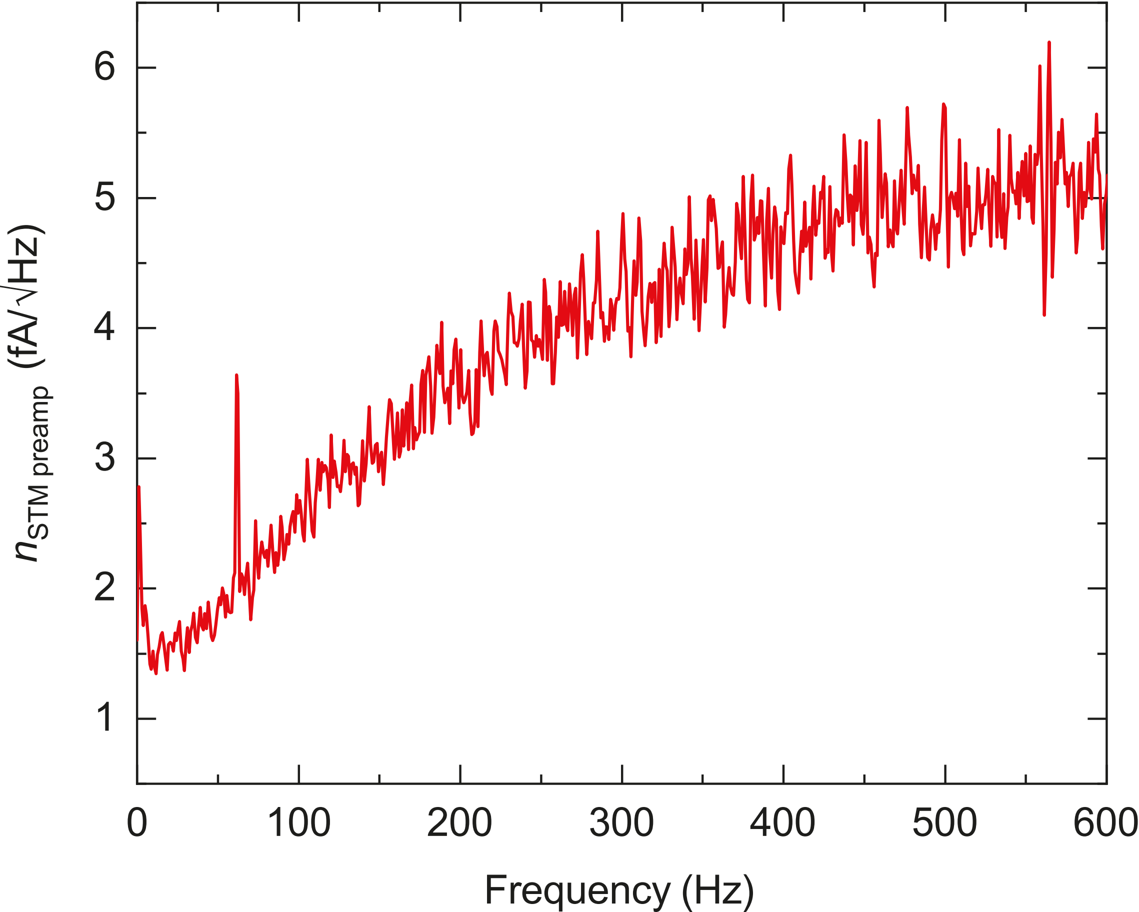

$n_{STM\ preamp}$ (fA/$\sqrt{Hz}$)
1
2
3
4
5
6
0
100
200
300
400
500
600
Frequency (Hz)

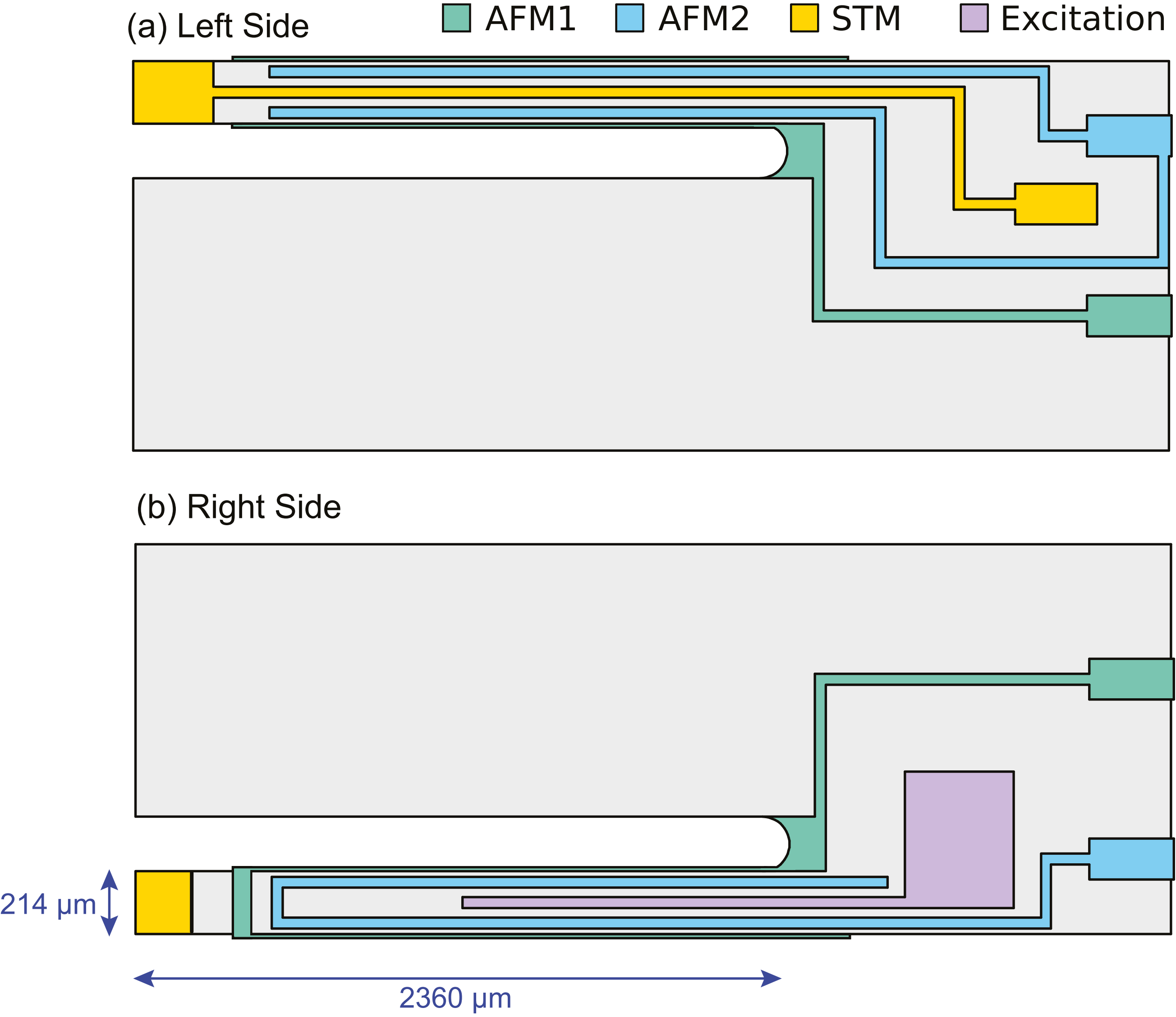
(a) Left Side
AFM1
AFM2
STM
Excitation
(b) Right Side
214 μm
2360 μm

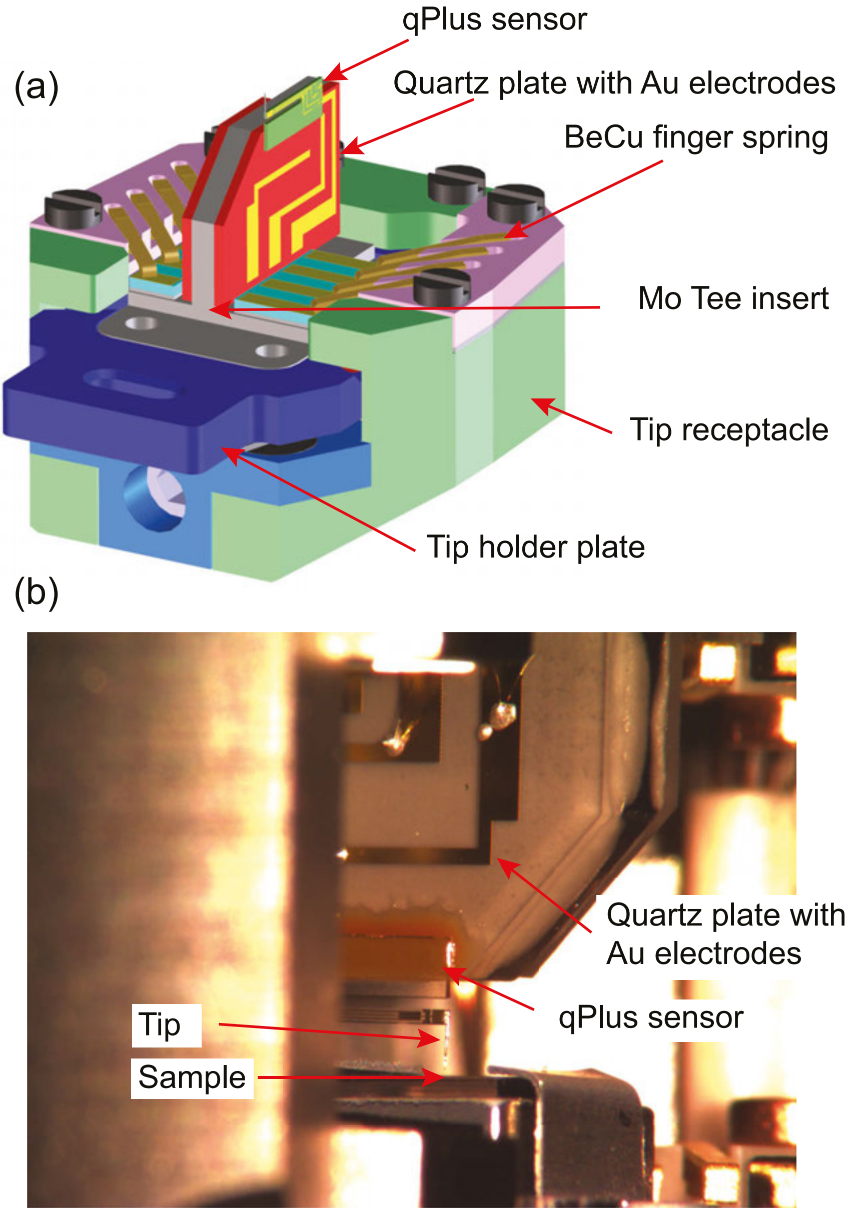
(a)
qPlus sensor
Quartz plate with Au electrodes
BeCu finger spring
Mo Tee insert
Tip receptacle
Tip holder plate
(b)
Quartz plate with
Au electrodes
qPlus sensor
Tip
Sample

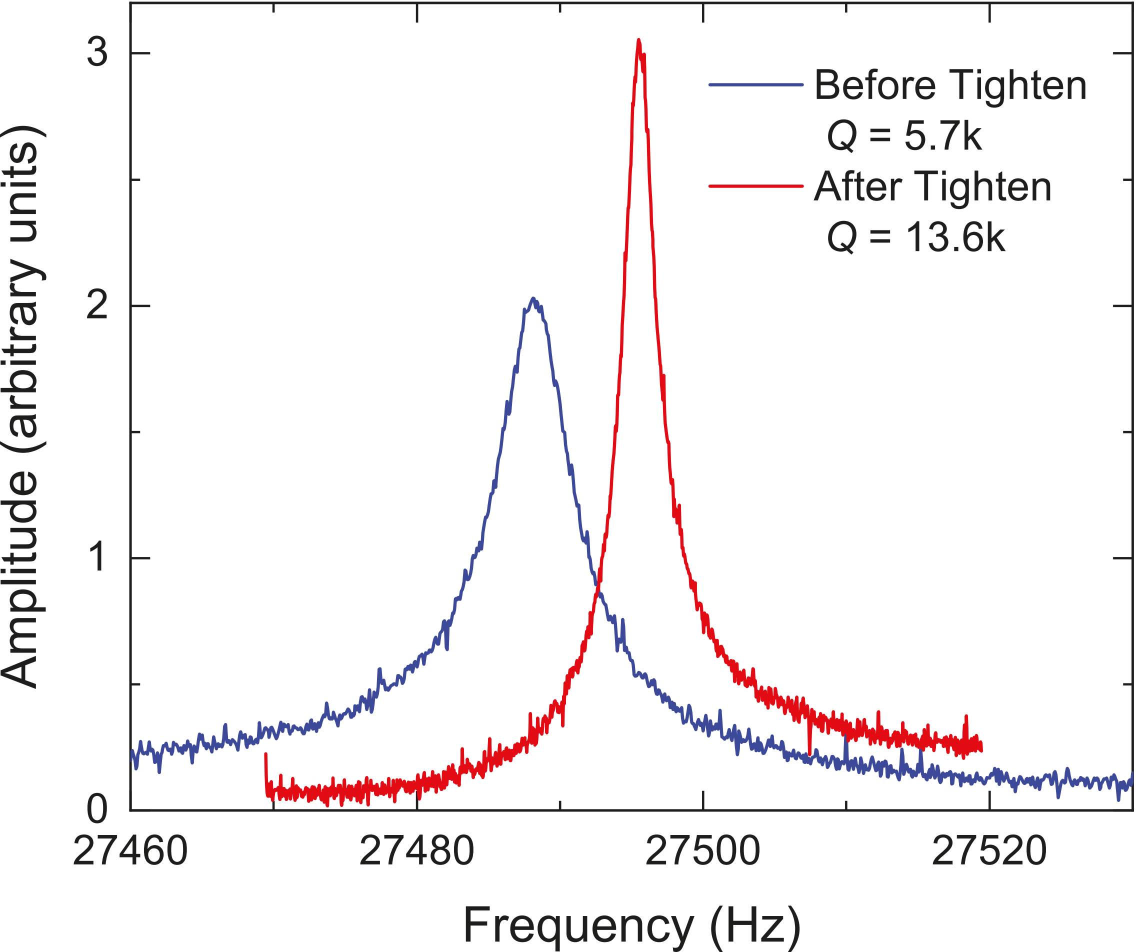

Before Tighten
Q = 5.7k
After Tighten
Q = 13.6k
Amplitude (arbitrary units)
Frequency (Hz)
0
1
2
3
27460
27480
27500
27520

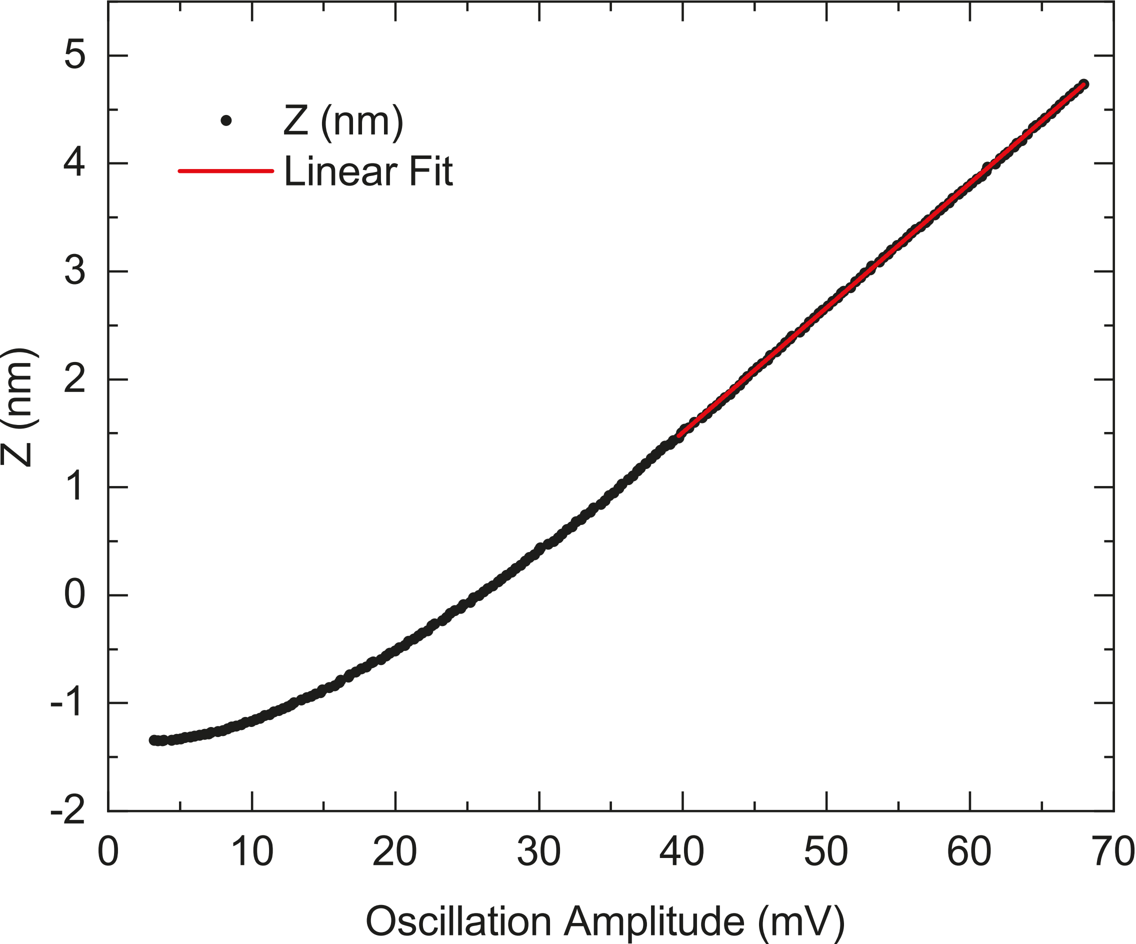

Z (nm)
Linear Fit
5
4
3
2
1
0
-1
-2
0
10
20
30
40
50
60
70
Z (nm)
Oscillation Amplitude (mV)

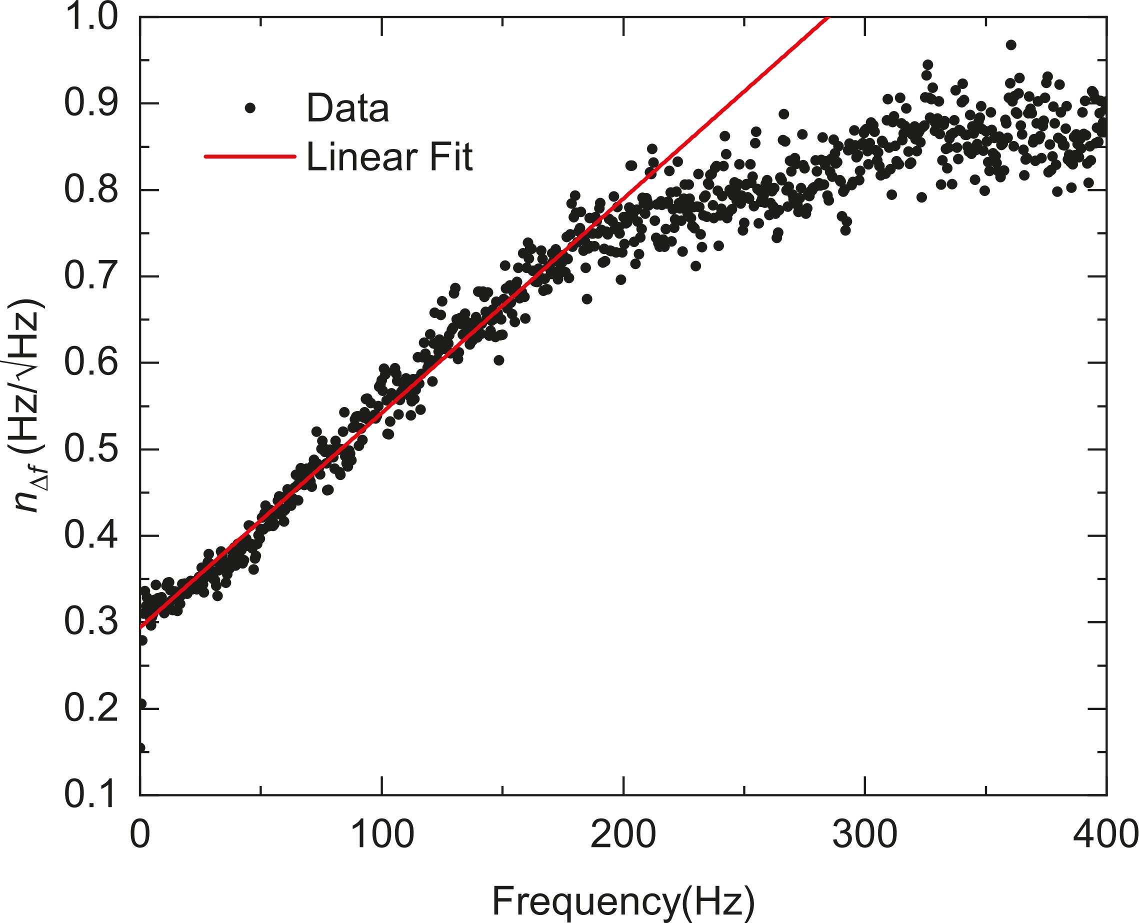

Data
Linear Fit
$n_{\Delta f}$ (Hz/√Hz)
Frequency(Hz)
1.0
0.9
0.8
0.7
0.6
0.5
0.4
0.3
0.2
0.1
0
100
200
300
400

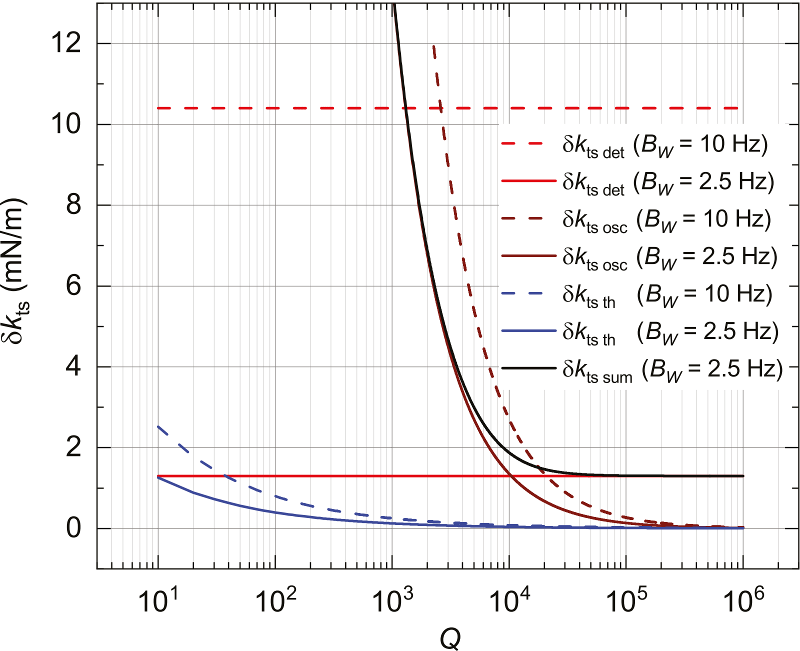

δk_{ts} (mN/m)
Q
0
2
4
6
8
10
12
10^1
10^2
10^3
10^4
10^5
10^6
$\delta k_{ts\ det}$ (B_W = 10 Hz)
$\delta k_{ts\ det}$ (B_W = 2.5 Hz)
$\delta k_{ts\ osc}$ (B_W = 10 Hz)
$\delta k_{ts\ osc}$ (B_W = 2.5 Hz)
$\delta k_{ts\ th}$ (B_W = 10 Hz)
$\delta k_{ts\ th}$ (B_W = 2.5 Hz)
$\delta k_{ts\ sum}$ (B_W = 2.5 Hz)

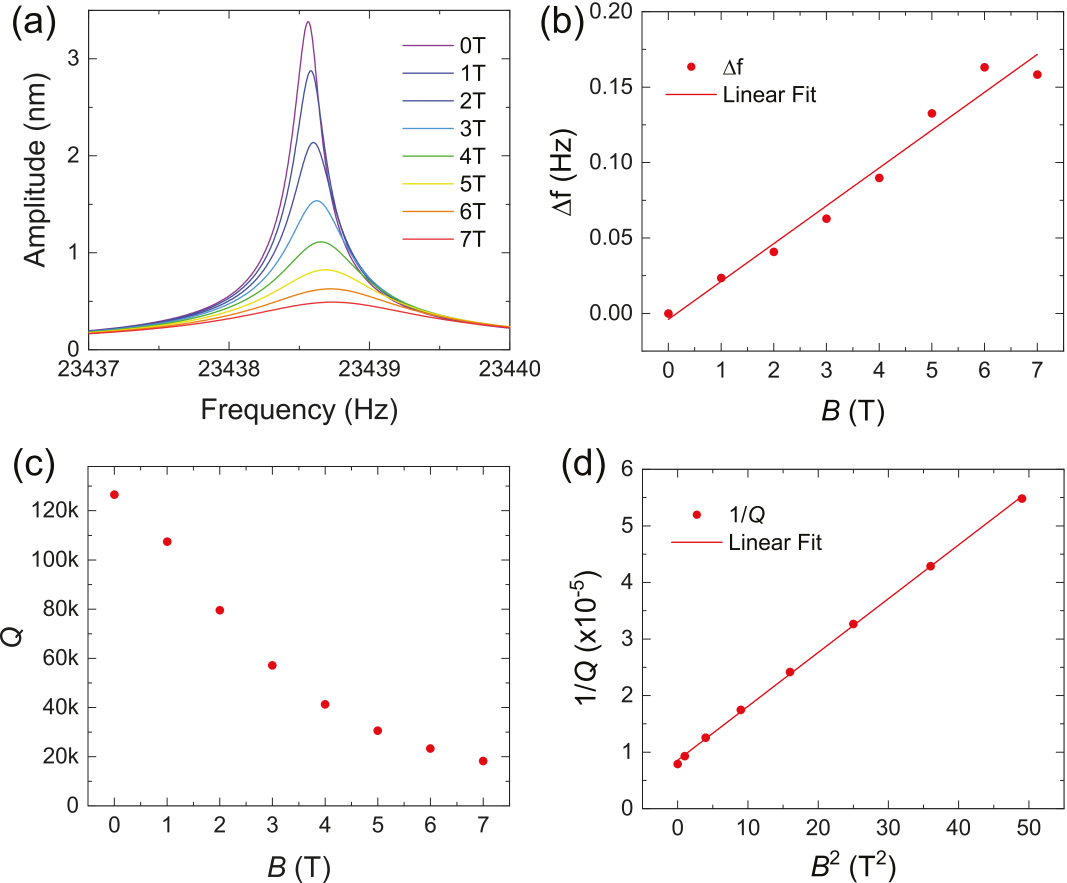

(a)
Amplitude (nm)
Frequency (Hz)
0T
1T
2T
3T
4T
5T
6T
7T
0
1
2
3
23437
23438
23439
23440
(b)
Δf (Hz)
B (T)
Δf
Linear Fit
0.00
0.05
0.10
0.15
0.20
0
1
2
3
4
5
6
7
(c)
Q
B (T)
0
20k
40k
60k
80k
100k
120k
0
1
2
3
4
5
6
7
(d)
1/Q (x10^-5)
B^2 (T^2)
1/Q
Linear Fit
0
1
2
3
4
5
6
0
10
20
30
40
50

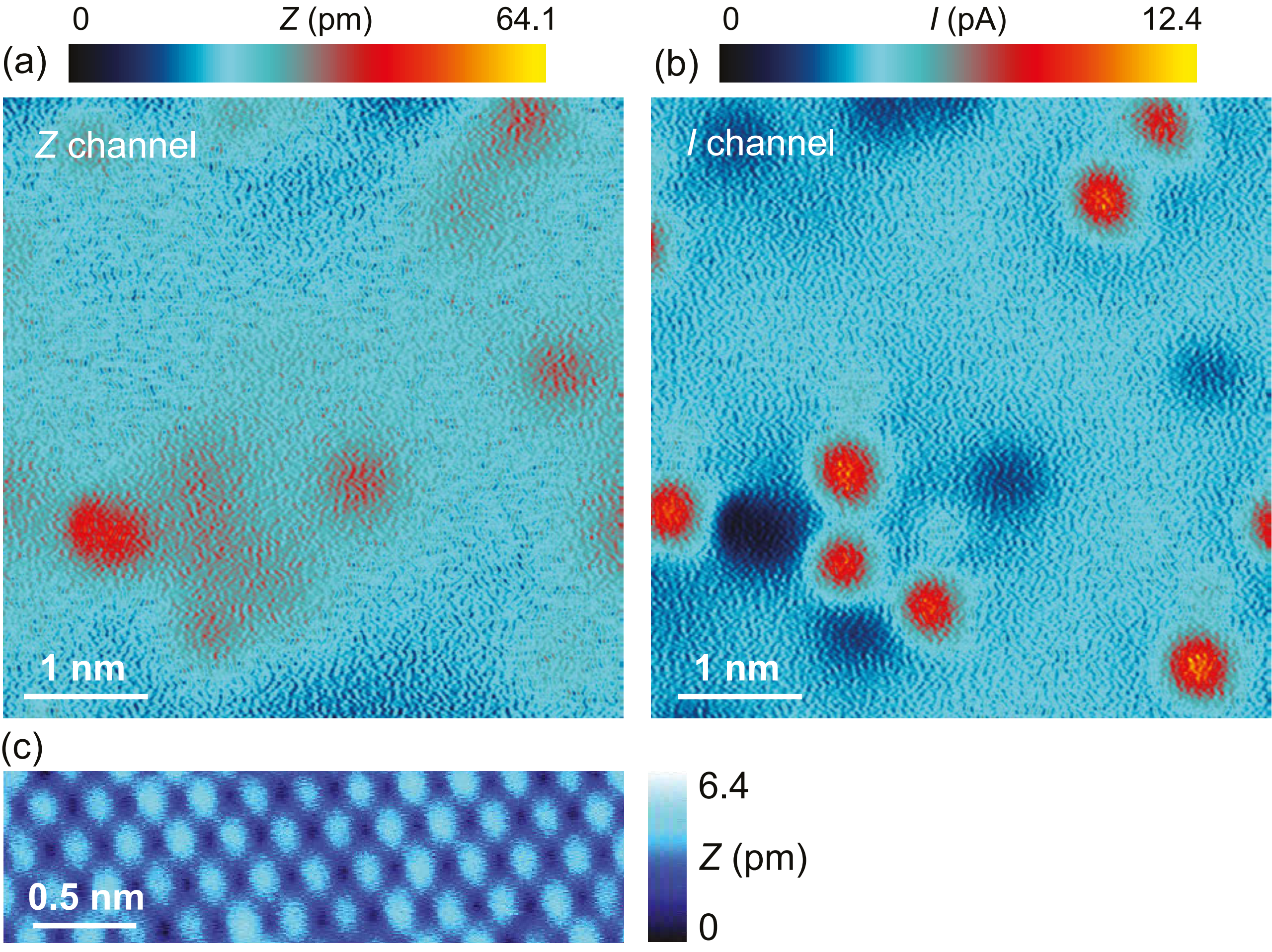

(a)
0
Z (pm)
64.1
Z channel
1 nm
(b)
0
I (pA)
12.4
I channel
1 nm
(c)
0.5 nm
6.4
Z (pm)
0

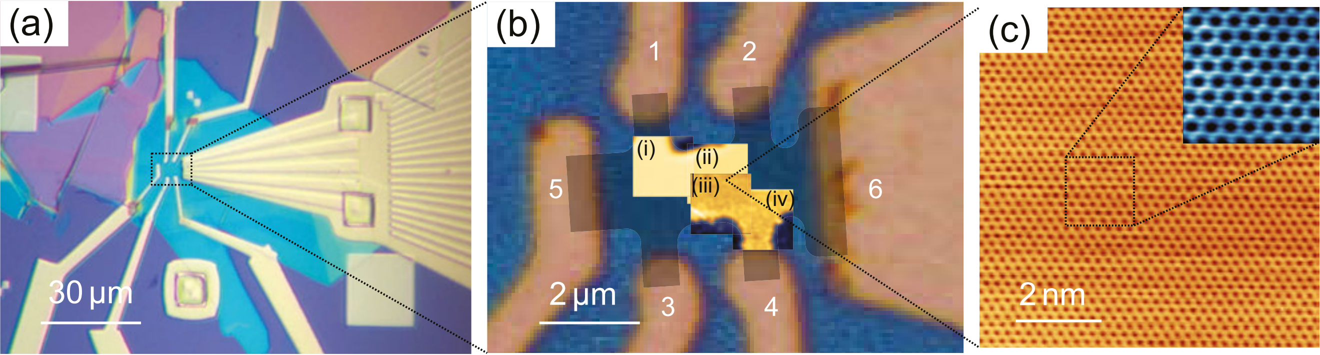

Figure 21: print full double column wide

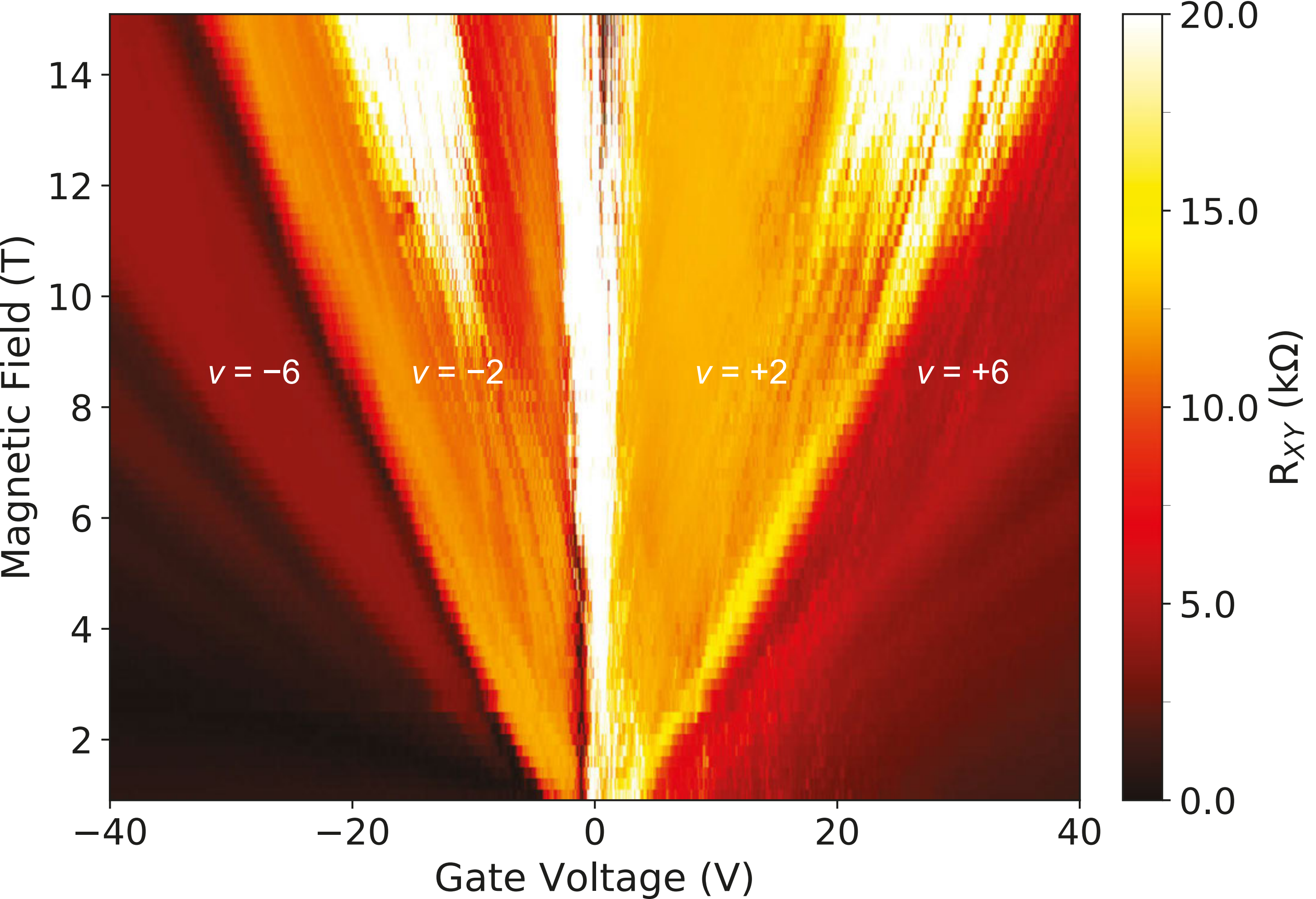

v = −6
v = −2
v = +2
v = +6
Magnetic Field (T)
Gate Voltage (V)
R_XY (kΩ)
−40
−20
0
20
40
2
4
6
8
10
12
14
0.0
5.0
10.0
15.0
20.0

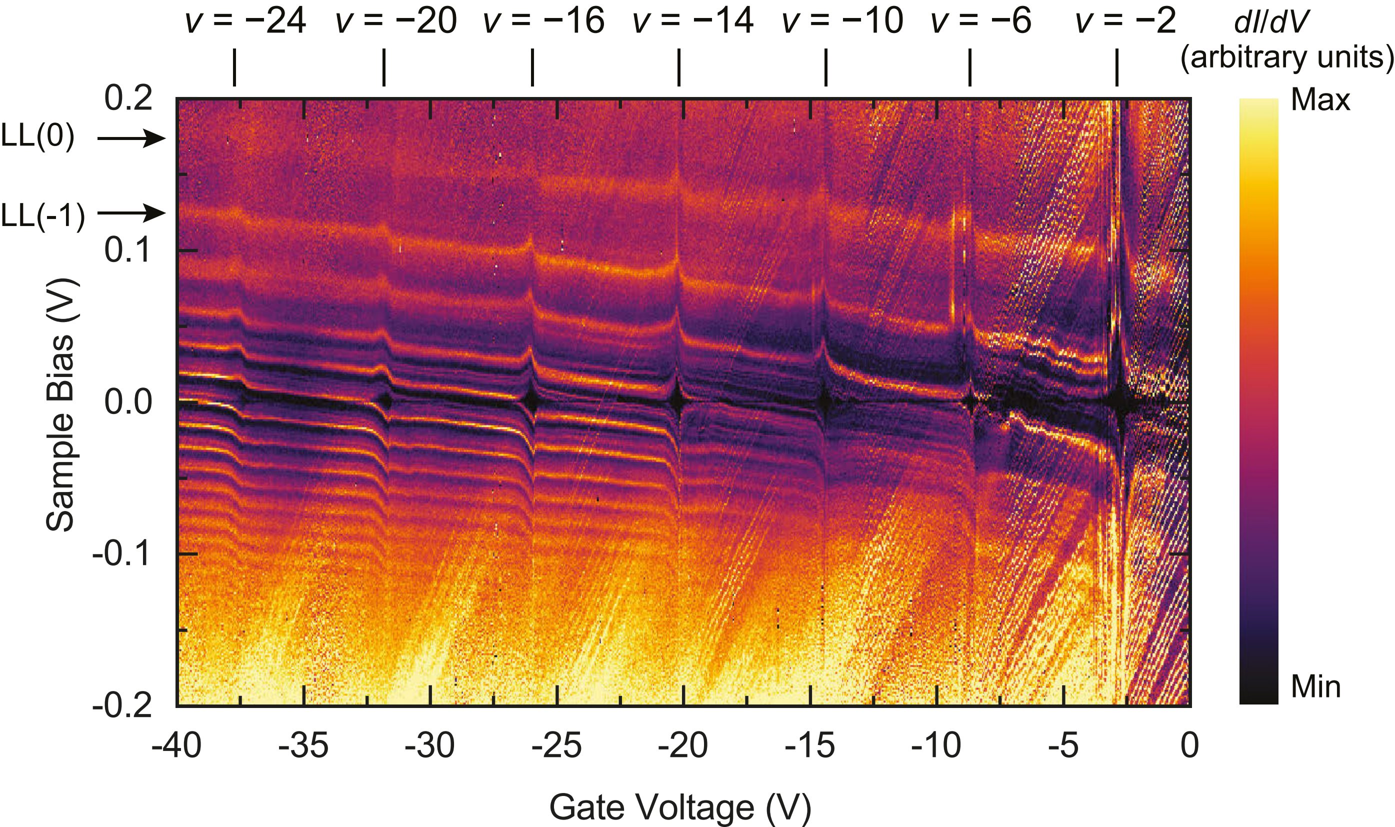

ν = −24
ν = −20
ν = −16
ν = −14
ν = −10
ν = −6
ν = −2
dI/dV
(arbitrary units)
Max
Min
LL(0)
LL(-1)
Sample Bias (V)
0.2
0.1
0.0
-0.1
-0.2
-40
-35
-30
-25
-20
-15
-10
-5
0
Gate Voltage (V)

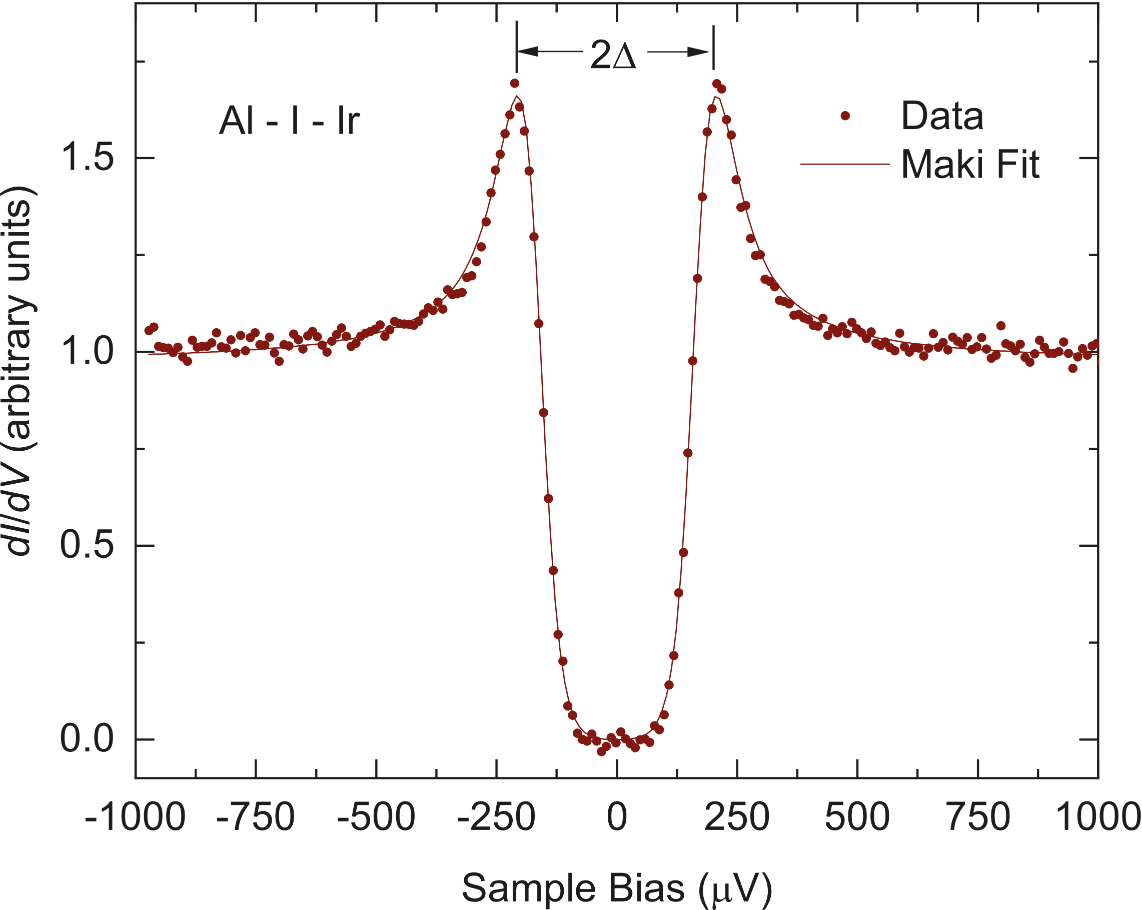
2Δ
Al - I - Ir
Data
Maki Fit
1.5
1.0
0.5
0.0
dI/dV (arbitrary units)
-1000
-750
-500
-250
0
250
500
750
1000
Sample Bias (μV)

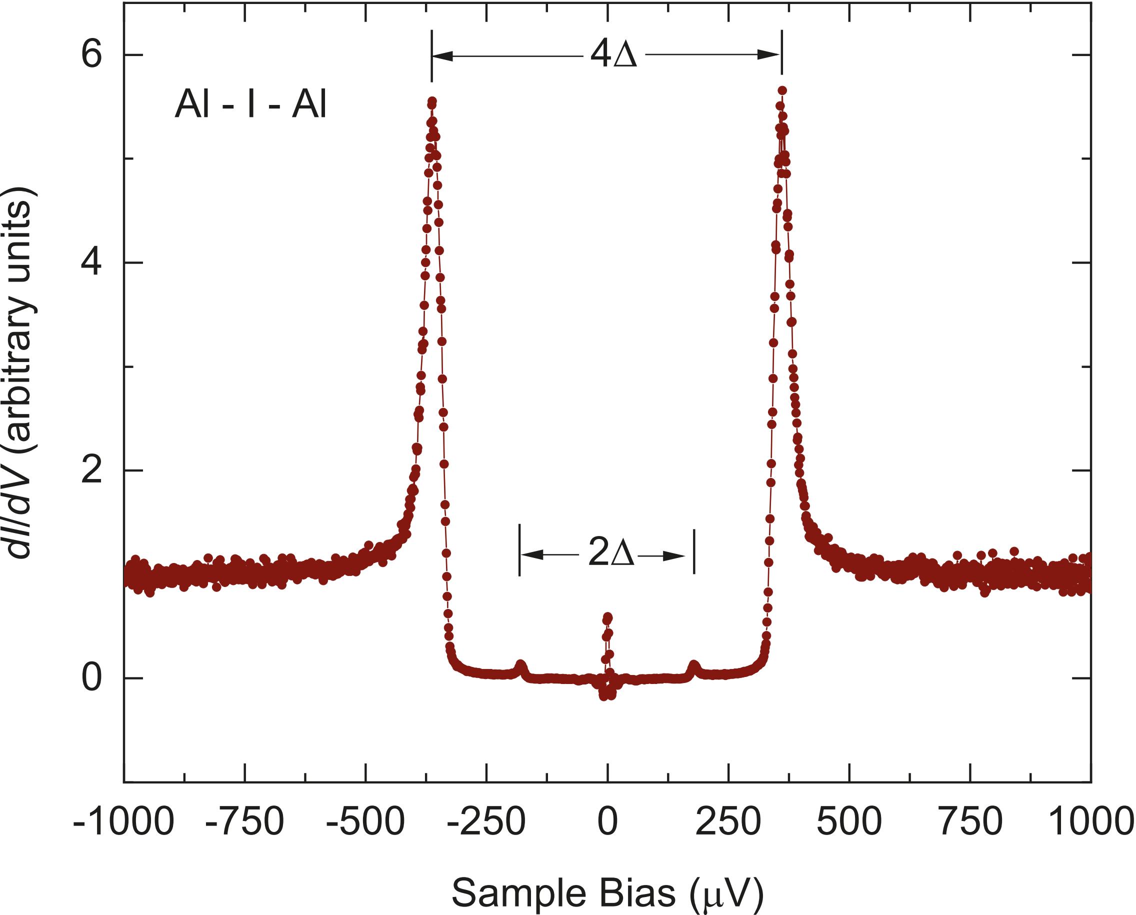

4Δ
Al - I - Al
2Δ
6
4
2
0
-1000
-750
-500
-250
0
250
500
750
1000
dI/dV (arbitrary units)
Sample Bias (μV)

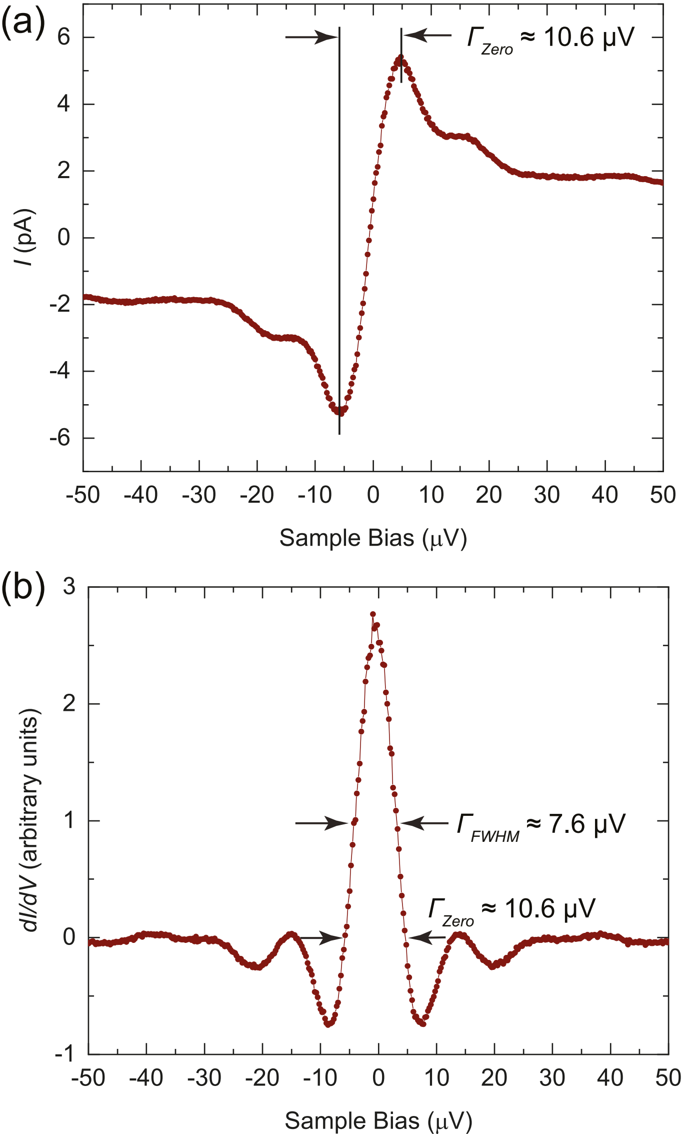

(a)
$\Gamma_{Zero} \approx 10.6\ \mu V$
6
4
2
0
-2
-4
-6
I (pA)
-50 -40 -30 -20 -10 0 10 20 30 40 50
Sample Bias (μV)
(b)
3
2
1
0
-1
dI/dV (arbitrary units)
$\Gamma_{FWHM} \approx 7.6\ \mu V$
$\Gamma_{Zero} \approx 10.6\ \mu V$
-50 -40 -30 -20 -10 0 10 20 30 40 50
Sample Bias (μV)

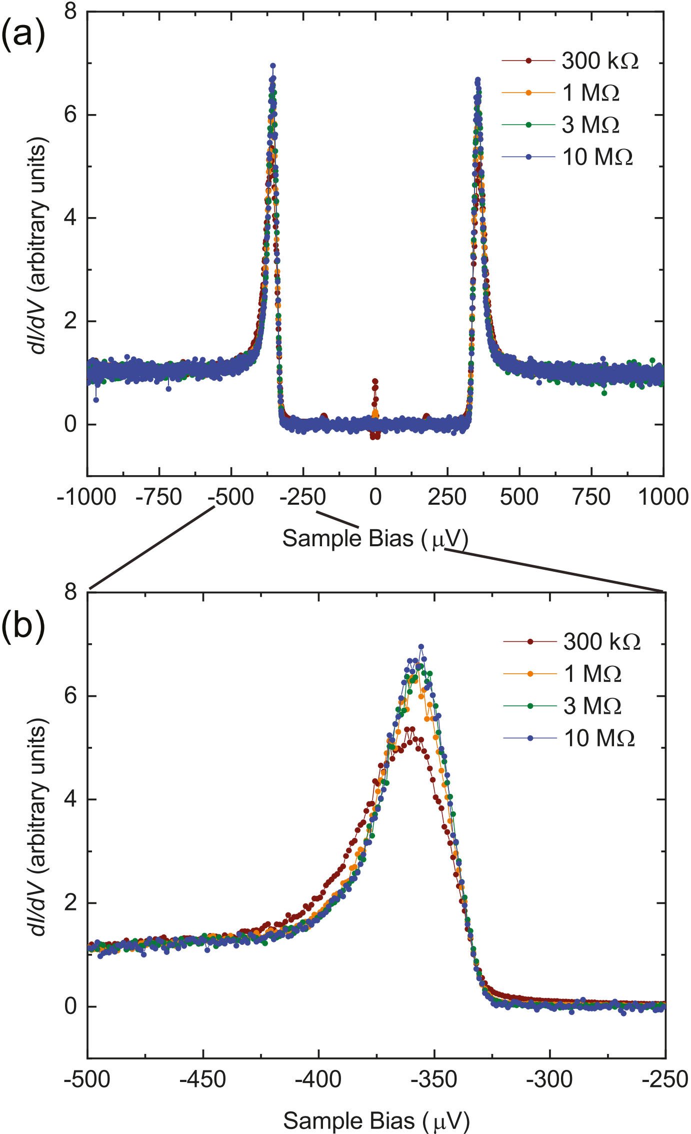

(a)
300 kΩ
1 MΩ
3 MΩ
10 MΩ
dI/dV (arbitrary units)
Sample Bias (μV)
(b)
300 kΩ
1 MΩ
3 MΩ
10 MΩ
dI/dV (arbitrary units)
Sample Bias (μV)

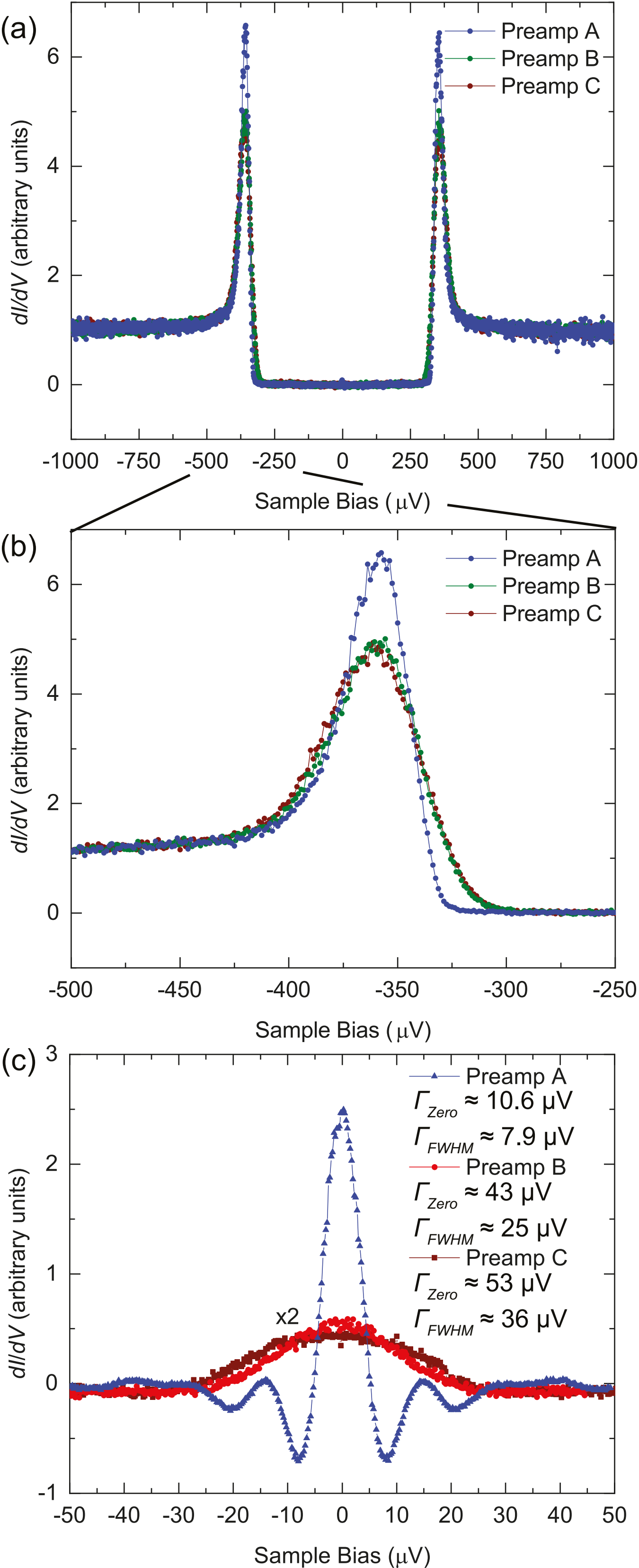

(a)
Preamp A
Preamp B
Preamp C
dI/dV (arbitrary units)
6
4
2
0
-1000
-750
-500
-250
0
250
500
750
1000
Sample Bias (μV)
(b)
Preamp A
Preamp B
Preamp C
dI/dV (arbitrary units)
6
4
2
0
-500
-450
-400
-350
-300
-250
Sample Bias (μV)
(c)
Preamp A
Γ_Zero ≈ 10.6 μV
Γ_FWHM ≈ 7.9 μV
Preamp B
Γ_Zero ≈ 43 μV
Γ_FWHM ≈ 25 μV
Preamp C
Γ_Zero ≈ 53 μV
Γ_FWHM ≈ 36 μV
x2
dI/dV (arbitrary units)
3
2
1
0
-1
-50
-40
-30
-20
-10
0
10
20
30
40
50
Sample Bias (μV)

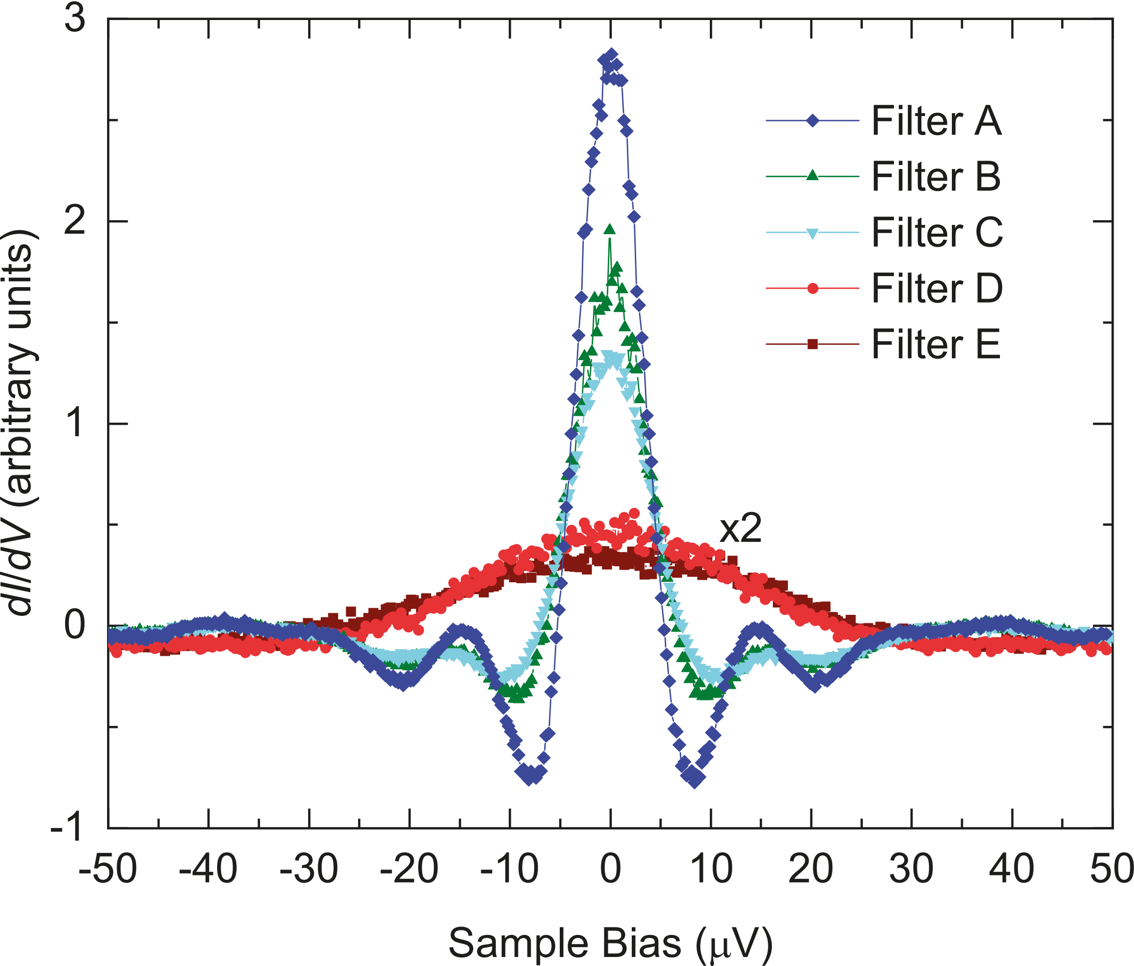

3
2
1
0
-1
dI/dV (arbitrary units)
-50
-40
-30
-20
-10
0
10
20
30
40
50
Sample Bias (μV)
Filter A
Filter B
Filter C
Filter D
Filter E
x2

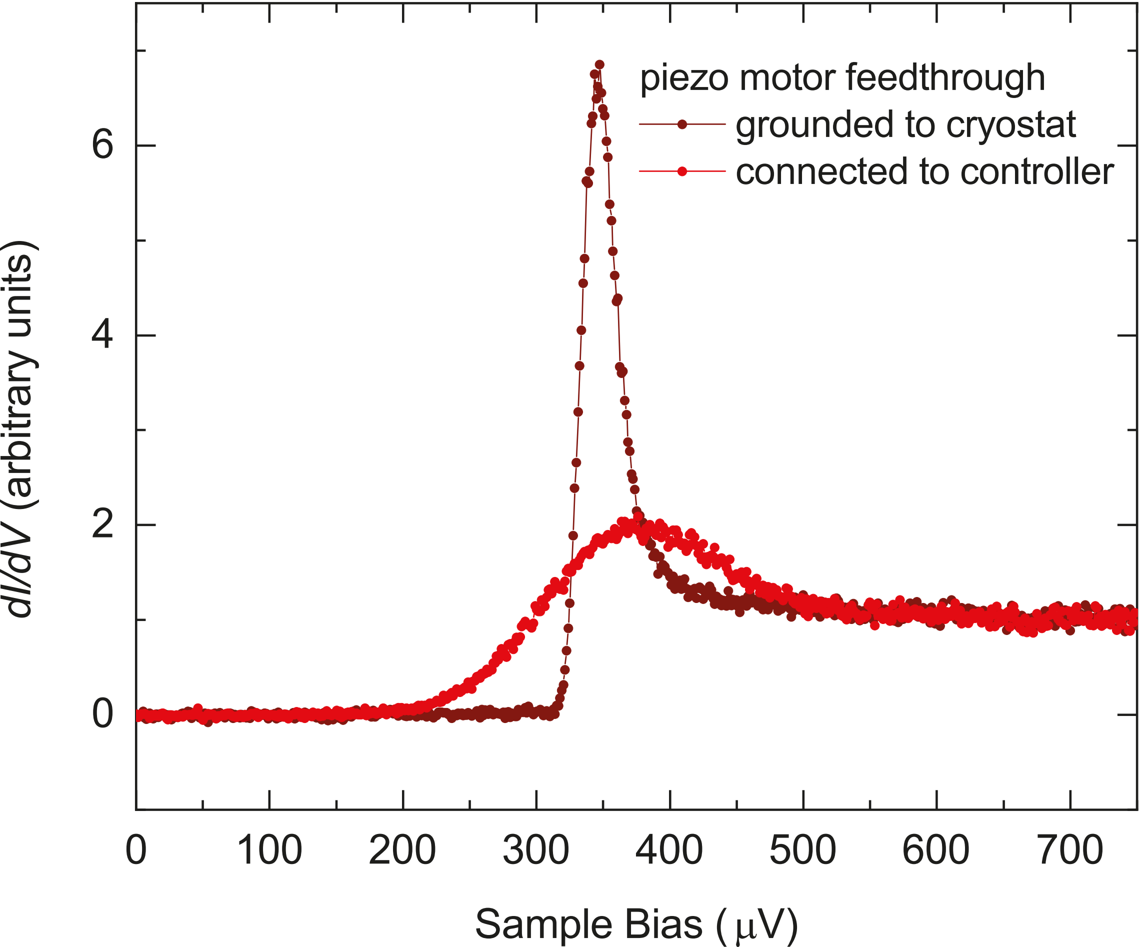

piezo motor feedthrough
grounded to cryostat
connected to controller
dI/dV (arbitrary units)
Sample Bias (μV)
0
2
4
6
0
100
200
300
400
500
600
700

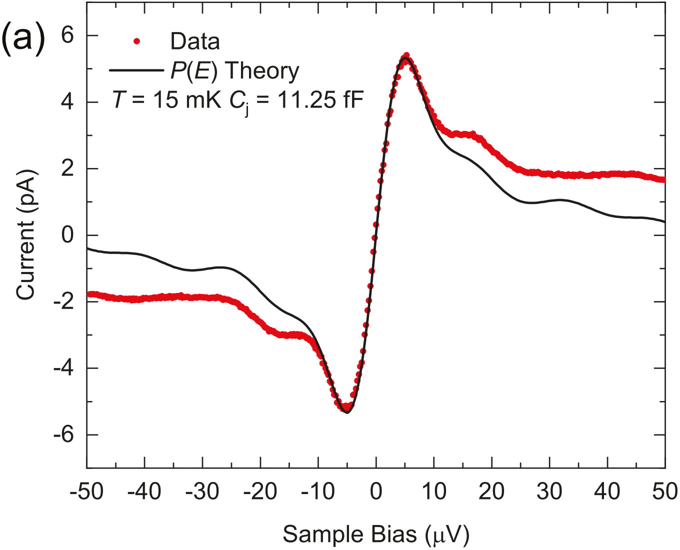
(a)
Data
P(E) Theory
T = 15 mK C_j = 11.25 fF
Current (pA)
6
4
2
0
-2
-4
-6
-50
-40
-30
-20
-10
0
10
20
30
40
50
Sample Bias (μV)

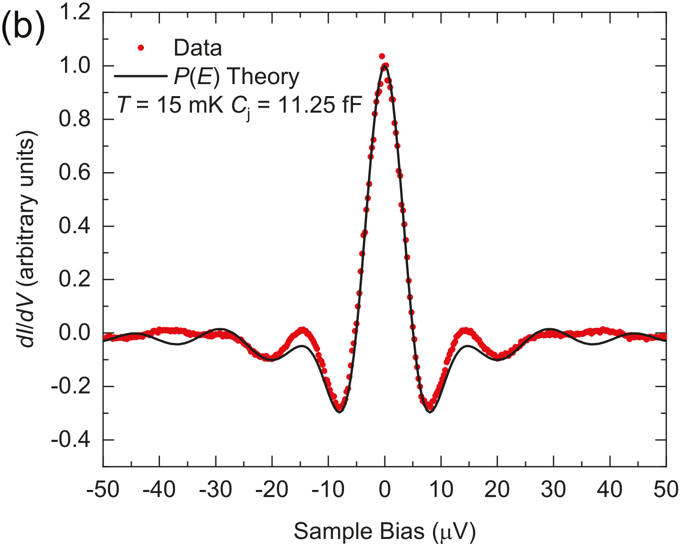
(b)
Data
P(E) Theory
T = 15 mK C_j = 11.25 fF
dI/dV (arbitrary units)
1.2
1.0
0.8
0.6
0.4
0.2
0.0
-0.2
-0.4
-50
-40
-30
-20
-10
0
10
20
30
40
50
Sample Bias (μV)

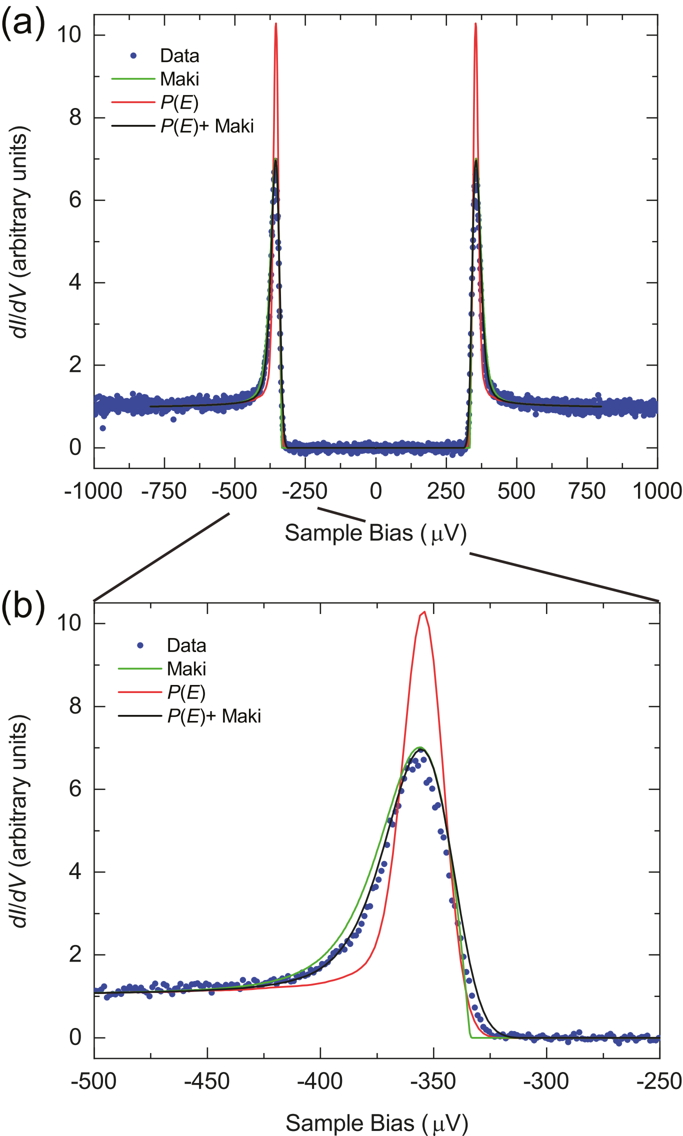
(a)
Data
Maki
P(E)
P(E)+ Maki
dI/dV (arbitrary units)
Sample Bias (μV)
(b)
Data
Maki
P(E)
P(E)+ Maki
dI/dV (arbitrary units)
Sample Bias (μV)

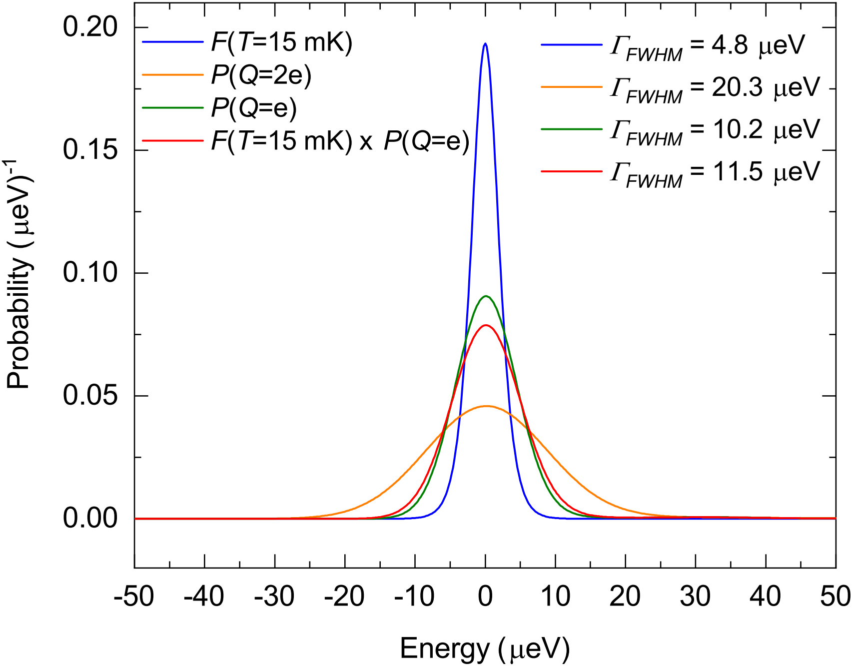

F(T=15 mK)
P(Q=2e)
P(Q=e)
F(T=15 mK) x P(Q=e)
Γ_FWHM = 4.8 μeV
Γ_FWHM = 20.3 μeV
Γ_FWHM = 10.2 μeV
Γ_FWHM = 11.5 μeV
Probability (μeV)^-1
Energy (μeV)
0.20
0.15
0.10
0.05
0.00
-50
-40
-30
-20
-10
0
10
20
30
40
50